

Galaxy-CMB and galaxy-galaxy lensing on large scales: sensitivity to primordial non-Gaussianity

Donghui Jeong* and Eiichiro Komatsu

*Texas Cosmology Center and Department of Astronomy,
University of Texas at Austin, 1 University Station, C1400, Austin, TX 78712*

Bhuvnesh Jain

*Particle Cosmology Center and Department of Physics and Astronomy,
University of Pennsylvania, Philadelphia, PA 19104*

A convincing detection of primordial non-Gaussianity in the local form of the bispectrum, whose amplitude is given by the f_{NL} parameter, offers a powerful test of inflation. In this paper we calculate the modification of two-point cross-correlation statistics of weak lensing - galaxy-galaxy lensing and galaxy-Cosmic Microwave Background (CMB) cross-correlation - due to f_{NL} . We derive and calculate the covariance matrix of galaxy-galaxy lensing including cosmic variance terms. We focus on large scales ($l < 100$) for which the shape noise of the shear measurement becomes irrelevant and cosmic variance dominates the error budget. For a modest degree of non-Gaussianity, $f_{\text{NL}} = \pm 50$, modifications of the galaxy-galaxy lensing signal at the 10% level are seen on scales $R \sim 300$ Mpc, and grow rapidly toward larger scales as $\propto R^2$. We also see a clear signature of the baryonic acoustic oscillation feature in the matter power spectrum at ~ 150 Mpc, which can be measured by next-generation lensing experiments. In addition we can probe the local-form primordial non-Gaussianity in the galaxy-CMB lensing signal by correlating the lensing potential reconstructed from CMB with high- z galaxies. For example, for $f_{\text{NL}} = \pm 50$, we find that the galaxy-CMB lensing cross power spectrum is modified by $\sim 10\%$ at $l \sim 40$, and by a factor of two at $l \sim 10$, for a population of galaxies at $z = 2$ with a bias of 2. The effect is greater for more highly biased populations at larger z ; thus, high- z galaxy surveys cross-correlated with CMB offer a yet another probe of primordial non-Gaussianity.

PACS numbers: 98.62.Sb; 98.65.-r; 98.80.-k

I. INTRODUCTION

Why study non-Gaussianity? For many years it was recognized that the simple inflationary models based upon a single slowly-rolling scalar field would predict nearly Gaussian primordial fluctuations. In particular, when we parametrize the magnitude of non-Gaussianity in the primordial curvature perturbations ζ , which gives the observed temperature anisotropy in the Cosmic Microwave Background (CMB) in the Sachs-Wolfe limit as $\Delta T/T = -\zeta/5$, using the so-called non-linear parameter f_{NL} [1] as $\zeta(\mathbf{x}) = \zeta_L(\mathbf{x}) + (3f_{\text{NL}}/5)\zeta_L^2(\mathbf{x})$, then the bispectrum of ζ is given by¹ $B_\zeta(k_1, k_2, k_3) = (6f_{\text{NL}}/5)[P_\zeta(k_1)P_\zeta(k_2) + (2 \text{ cyclic terms})]$, where $P_\zeta(k) \propto k^{n_s-4}$ is the power spectrum of ζ and n_s is the tilt of the power spectrum, constrained as $n_s = 0.960 \pm 0.013$ by the WMAP 5-year data [2]. This form of the bispectrum has the maximum signal in the so-called squeezed triangle for which $k_3 \ll k_2 \approx k_1$ [3]. In this limit we obtain

$$B_\zeta(k_1, k_1, k_3 \rightarrow 0) = \frac{12}{5}f_{\text{NL}}P_\zeta(k_1)P_\zeta(k_3). \quad (1)$$

The earlier calculations showed that f_{NL} from single-field slow-roll inflation would be of order the slow-roll parameter, $\epsilon \sim 10^{-2}$ [4, 5, 6]. However, it is not until recent that it is finally realized that the coefficient of $P_\zeta(k_1)P_\zeta(k_3)$ from the simplest single-field slow-roll inflation with the canonical kinetic term in the squeezed limit is given precisely by [7, 8]

$$B_\zeta(k_1, k_1, k_3 \rightarrow 0) = (1 - n_s)P_\zeta(k_1)P_\zeta(k_3). \quad (2)$$

Comparing this result with the form predicted by the f_{NL} model, one obtains $f_{\text{NL}} = (5/12)(1 - n_s)$.

Perhaps, the most important theoretical discovery regarding primordial non-Gaussianity from inflation over the last few years is that, not only models with the canonical kinetic term, but *all* single-inflation models predict the bispectrum in the squeezed limit given by Eq. (2), regardless of the form of potential, kinetic term, slow-roll, or initial vacuum state [9, 10, 11, 12]. Therefore, the prediction from all single-field inflation models is $f_{\text{NL}} = (5/12)(1 - n_s) = 0.017$ for $n_s = 0.96$. A convincing detection of f_{NL} well above this level is a breakthrough in our understanding of the physics of very early universe [13, 14]. The current limit from the WMAP 5-year data is $f_{\text{NL}} = 38 \pm 21$ (68% CL) [15].

There are many ways of measuring f_{NL} . The most popular method has been the bispectrum of CMB [1, 16, 17, 18, 19] (also see [20] for a pedagogical review). The other methods include the trispectrum of CMB [21,

*Electronic address: djeong@astro.as.utexas.edu

¹ Definition of the bispectrum in terms of Fourier coefficients of ζ is $\langle \zeta_{\mathbf{k}_1} \zeta_{\mathbf{k}_2} \zeta_{\mathbf{k}_3} \rangle = (2\pi)^3 \delta(\mathbf{k}_1 + \mathbf{k}_2 + \mathbf{k}_3) B_\zeta(k_1, k_2, k_3)$. Throughout this paper we shall order k_i such that $k_3 \leq k_2 \leq k_1$.

22], the bispectrum of galaxies [23, 24, 25, 26], and the abundance of galaxies and clusters of galaxies [27, 28, 29, 30].

Recently, analytical [31, 32, 33, 34, 35] and numerical [31, 36, 37, 38] studies of the effects of primordial non-Gaussianity on the power spectrum of dark matter halos, $P_h(k)$, have revealed an unexpected signature of primordial non-Gaussianity in the form of a *scale-dependent galaxy bias*, i.e., $P_h(k) = b_1^2 P_m(k) \rightarrow [b_1 + \Delta b(k)]^2 P_m(k)$, where $P_m(k)$ is the power spectrum of matter density fluctuations, and

$$\Delta b(k) = \frac{3(b_1 - 1)f_{\text{NL}}\Omega_m H_0^2 \delta_c}{D(z)k^2 T(k)}. \quad (3)$$

Here, $D(z)$ and $T(k)$ are the growth rate and the transfer function for linear matter density fluctuations, respectively, and $\delta_c = 1.68$ is the threshold linear density contrast for a spherical collapse of an overdensity region. The k^2 factor in the denominator of $\Delta b(k)$ shows that this effect is important only on very large scales. Highly biased tracers are more sensitive to f_{NL} .

II. HALO-MASS CORRELATION FROM GALAXY-GALAXY LENSING

A. Formula

The scale-dependent bias was theoretically discovered when the authors of [31] studied the form of the *cross-correlation* power spectrum between the dark matter halos and the underlying matter density fluctuations, $P_{hm}(k) = [b_1 + \Delta b(k)]P_m(k)$. We can observe $P_{hm}(k)$ by cross-correlating the locations of galaxies or clusters of galaxies with the matter density fluctuations traced by the weak gravitational lensing (see [39] for a review).

One efficient way of measuring $P_{hm}(k)$ is to use the so-called galaxy-galaxy lensing technique [40, 41, 42, 43, 44, 45, 46]: choose one lens galaxy at a redshift z_L , and measure the mean of *tangential* shears in images of lensed (source or background) galaxies around the chosen central lensing galaxy as a function of radii from that central galaxy. Finally, average those mean tangential shears over all lensing galaxies at the same redshift, z_L .

We begin with the definition of the tangential shear, γ_t , on the flat sky²

$$\gamma_t(\boldsymbol{\theta}) = -\gamma_1(\boldsymbol{\theta}) \cos(2\phi) - \gamma_2(\boldsymbol{\theta}) \sin(2\phi), \quad (4)$$

where $\boldsymbol{\theta} = (\theta \cos \phi, \theta \sin \phi)$, and γ_1 and γ_2 are components of the shear field.³ The coordinate system and

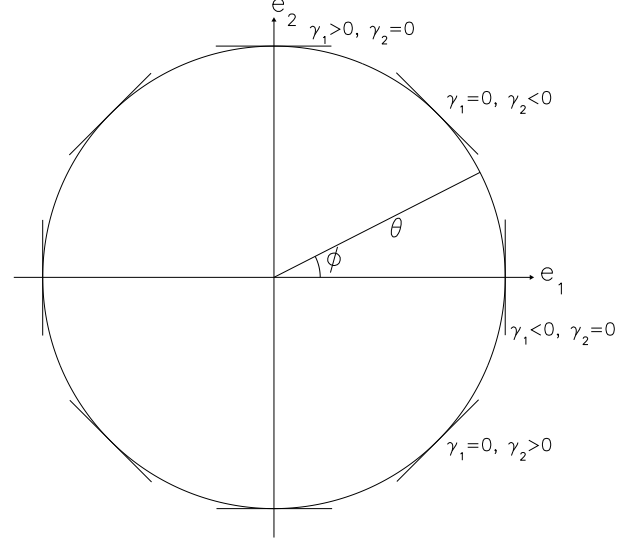


FIG. 1: Coordinate system and γ_1 and γ_2 . The shear along e_1 has $\gamma_1 > 0$ and $\gamma_2 = 0$, whereas the shear along e_2 has $\gamma_1 < 0$ and $\gamma_2 = 0$. The shear along $e_1 + e_2$ has $\gamma_1 = 0$ and $\gamma_2 > 0$, whereas The shear along $e_1 - e_2$ has $\gamma_1 = 0$ and $\gamma_2 < 0$.

the meaning of γ_1 and γ_2 are explained in Fig. 1. For purely tangential shears shown in Fig. 1, γ_t is always positive. This property allows us to average γ_t over the ring around the origin to estimate the mean tangential shear, $\bar{\gamma}_t$:

$$\bar{\gamma}_t(\theta) \equiv \int_0^{2\pi} \frac{d\phi}{2\pi} \gamma_t(\theta, \phi). \quad (5)$$

On the flat sky, γ_1 and γ_2 are related to the projected mass density fluctuation in Fourier space, $\kappa(\mathbf{l})$, as

$$\gamma_1(\boldsymbol{\theta}) = \int \frac{d^2 \mathbf{l}}{(2\pi)^2} \kappa(\mathbf{l}) \cos(2\varphi) e^{i\mathbf{l} \cdot \boldsymbol{\theta}}, \quad (6)$$

$$\gamma_2(\boldsymbol{\theta}) = \int \frac{d^2 \mathbf{l}}{(2\pi)^2} \kappa(\mathbf{l}) \sin(2\varphi) e^{i\mathbf{l} \cdot \boldsymbol{\theta}}, \quad (7)$$

where φ is the angle between \mathbf{l} and \mathbf{e}_1 , i.e., $\mathbf{l} = (l \cos \varphi, l \sin \varphi)$. Using Eqs. (6) and (7) in Eq. (4), we write the tangential shear in terms of $\kappa(\mathbf{l})$ as

$$\gamma_t(\boldsymbol{\theta}) = - \int \frac{d^2 \mathbf{l}}{(2\pi)^2} \kappa(\mathbf{l}) \cos[2(\phi - \varphi)] e^{i\mathbf{l} \cdot \boldsymbol{\theta}} \cos(\phi - \varphi). \quad (8)$$

tangential shear. In particular, on large scales there is information in the other component of the shear, and thus the full analysis including both shear components (not just tangential one) yields a modest (smaller than a factor of $\sqrt{2}$) improvement in the signal-to-noise ratio. Moreover, using magnification (in addition to shears), which is proportional to the convergence field κ , can also yield a modest improvement.

² For an all-sky analysis, this relation needs to be replaced with the exact relation using the spin-2 harmonics [47].

³ As the shear has two independent components, we are ignoring another linear combination of γ_1 and γ_2 by only focusing on the

The mean tangential shear (Eq. (5)) is then given by

$$\begin{aligned}\bar{\gamma}_t(\theta) &= - \int \frac{d^2\mathbf{l}}{(2\pi)^2} \kappa(\mathbf{l}) \int_0^{2\pi} \frac{d\phi}{2\pi} \cos[2(\phi - \varphi)] e^{il\theta \cos(\phi - \varphi)} \\ &= \int \frac{d^2\mathbf{l}}{(2\pi)^2} \kappa(\mathbf{l}) J_2(l\theta).\end{aligned}\quad (9)$$

Here, we have used the identity

$$J_m(x) = \int_{\alpha}^{2\pi+\alpha} \frac{d\psi}{2\pi} e^{i(m\psi - x \sin \psi)}, \quad (10)$$

with $m = 2$, $\psi = \phi - \varphi - \pi/2$, $\alpha = \varphi + \pi/2$, and $\int_0^{2\pi} d\psi \sin(2\psi) e^{ix \cos \psi} = 0$.

The ensemble average of the mean tangential shear vanishes, i.e., $\langle \bar{\gamma}_t \rangle = 0$, as $\langle \kappa \rangle = 0$. This simply means that the average of the mean tangential shears, measured with respect to random points on the sky, vanishes. We obtain non-zero values when we average the mean tangential shears measured with respect to the locations of halos (galaxies or clusters of galaxies). This quantity, called the galaxy-galaxy lensing or cluster-galaxy lensing, can be used to measure the halo-mass cross correlation.

While clusters of galaxies may be identified directly with dark matter halos of a given mass, how are galaxies related to halos? Some galaxies (“field galaxies”) may also be identified directly with dark matter halos; however, galaxies residing within groups or clusters of galaxies should be identified with subhalos moving in a bigger dark matter halo. For such subhalos our argument given below may not be immediately used. However, it is observationally feasible to identify the central galaxies in groups or clusters of galaxies and measure the mean tangential shear around them. A number of studies of Luminous Red Galaxies (LRGs) extracted from the Sloan Digital Sky Survey (SDSS) have shown that these are typical central galaxies in galaxy groups [46, 48, 49]. Scalings such as the mass-luminosity scaling imply that LRGs provide a useful proxy for the halos within which they reside. We will assume in this study that such tracers will enable the halo-shear cross-correlation to be measured. There are some caveats such as bimodal mass distributions in galaxy groups [49] and the extrapolation to higher redshift, but we will leave a detailed exploration to real galaxy tracers for later work.

The ensemble average of the mean tangential shears relative to the locations of halos at a given redshift z_L , denoted as $\langle \bar{\gamma}_t^h \rangle(\theta, z_L)$, is related to the angular cross-correlation power spectrum of halos and κ , $C_l^{h\kappa}$, as [50]

$$\langle \bar{\gamma}_t^h \rangle(\theta, z_L) = \int \frac{l dl}{2\pi} C_l^{h\kappa}(z_L) J_2(l\theta). \quad (11)$$

We give the derivation of this result in Appendix A.

With the lens redshift z_L known (from spectroscopic observations), we can calculate the comoving radius, R , corresponding to the angular separation on the sky, θ , as $R = \theta d_A(0; z_L)$ where $d_A(0; z_L)$ is the *comoving* angular diameter distance from $z = 0$ to $z = z_L$. Using Limber’s

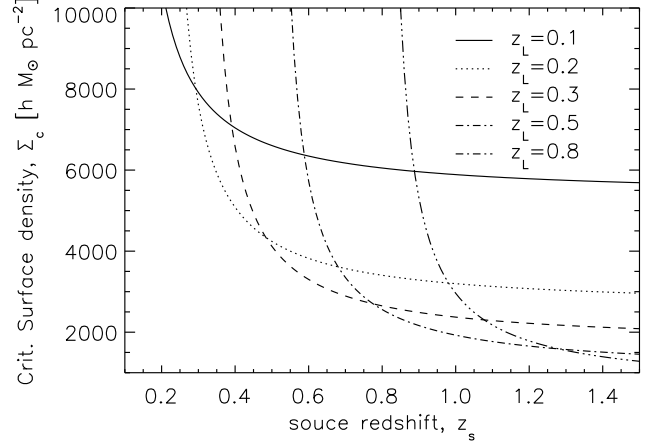


FIG. 2: Critical surface density, $\Sigma_c(z_L; z_s)$, as a function of the source redshift, z_s , for various lens redshifts that roughly correspond to the Two Degree Field Galaxy Redshift Survey (2dFGRS; $z_L = 0.1$, solid), the main sample of the Sloan Digital Sky Survey (SDSS; $z_L = 0.2$, dotted), the Luminous Red Galaxies (LRGs) of SDSS ($z_L = 0.3$, dashed), and the Large Synoptic Survey Telescope (LSST; $z_L = 0.5$ and 0.8 , dot-dashed and triple-dot-dashed, respectively).

approximation [51, 52] on the flat sky relating $C_l^{h\kappa}$ to $P_{hm}(k)$,⁴ we can write Eq. (11) as [50]

$$\langle \bar{\gamma}_t^h \rangle(R, z_L) = \frac{\rho_0}{\Sigma_c(z_L)} \int \frac{k dk}{2\pi} P_{hm}(k, z_L) J_2(kR). \quad (12)$$

Here, ρ_0 is the mean comoving mass density of the universe, and $\Sigma_c(z_L)$ is the so-called critical surface density:

$$\Sigma_c^{-1}(z_L) = \frac{4\pi G}{c^2} (1+z_L) d_A(0; z_L) \int_{z_L}^{\infty} dz_s p(z_s) \frac{d_A(z_L; z_s)}{d_A(0; z_s)}, \quad (13)$$

where $p(z_s)$ is the redshift distribution of sources normalized to unity, $\int dz p(z) = 1$, and $d_A(0; z)$ and $d_A(z; z_s)$ are the comoving angular diameter distances out to z and between z and z_s , respectively. The numerical value of $4\pi G/c^2$ is 6.01×10^{-19} Mpc/ M_\odot , and $4\pi G\rho_0/c^2$ is $1.67 \times 10^{-7} (\Omega_m h^2)$ Mpc $^{-2}$.

Eq. (12) is often written as

$$\langle \bar{\gamma}_t^h \rangle(R, z_L) = \frac{\Delta \Sigma(R, z_L)}{\Sigma_c(z_L)}. \quad (14)$$

To simplify the analysis, let us define the “effective source redshift” of a given survey from the following equation:

$$\frac{d_A(z_L; z_{s,\text{eff}})}{d_A(0; z_{s,\text{eff}})} \equiv \int_{z_L}^{\infty} dz_s p(z_s) \frac{d_A(z_L; z_s)}{d_A(0; z_s)}. \quad (15)$$

⁴ As we are dealing with correlations on very large angular scales, one may worry about the validity of Limber’s approximation. In Appendix C we give a detailed study of the validity and limitation of Limber’s approximation for the galaxy-galaxy lensing.

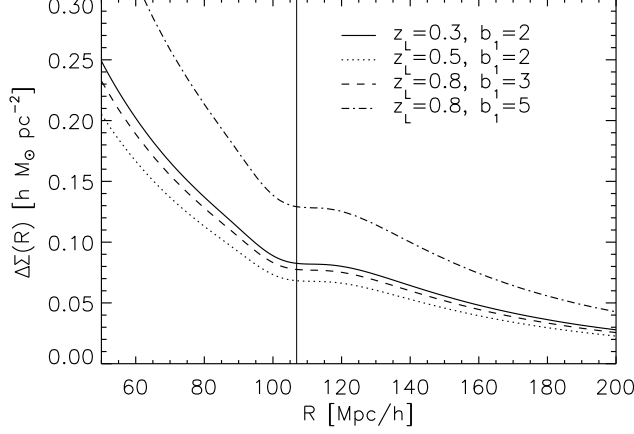


FIG. 3: The baryonic feature in the matter power spectrum, as seen in the galaxy-galaxy lensing, $\Delta\Sigma(R)$, for several populations of lens galaxies with $b_1 = 2$ at $z_L = 0.3$ (similar to SDSS LRGs, solid), $b_1 = 2$ at $z_L = 0.5$ (higher- z LRGs, dotted), $b_1 = 2$ at $z_L = 0.8$ (galaxies that can be observed by LSST, dashed), and $b_1 = 5$ at $z_L = 0.8$ (clusters of galaxies that can be observed by LSST, dot-dashed). The vertical line shows the location of the baryonic feature, $R_{\text{BAO}} = 106.9 h^{-1} \text{ Mpc}$, calculated from the “WMAP+BAO+SN ML” parameters in Table 1 of [2]. Note that we have used the linear matter power spectrum and the Gaussian initial condition ($f_{\text{NL}} = 0$) for this calculation.

Henceforth we shall use z_S to denote $z_{S,\text{eff}}$, and write

$$\Sigma_c^{-1}(z_L; z_S) = \frac{4\pi G}{c^2} (1 + z_L) d_A(0; z_L) \frac{d_A(z_L; z_S)}{d_A(0; z_S)}. \quad (16)$$

Fig. 2 shows Σ_c for $z_L = 0.1$ (2dFGRS, Two Degree Field Galaxy Redshift Survey), 0.2 (SDSS main), 0.3 (SDSS LRG), and 0.5 and 0.8 (both LSST, Large Synoptic Survey Telescope). The smaller Σ_c is, the larger the observed mean tangential shear is.

B. Results

We can now calculate the observable, $\Delta\Sigma(R, z_L)$, for various values of f_{NL} . We use

$$\begin{aligned} \Delta\Sigma(R, z_L) &= \rho_0 b_1 \int \frac{k dk}{2\pi} P_m(k, z_L) J_2(kR) \\ &\quad + \rho_0 \int \frac{k dk}{2\pi} \Delta b(k, z_L) P_m(k, z_L) J_2(kR), \end{aligned} \quad (17)$$

where the scale-dependent bias, $\Delta b(k, z)$, is given by Eq. (3). As we are interested in large scales, i.e., $R > 10 h^{-1} \text{ Mpc}$, we shall use the linear matter spectrum for $P_m(k)$.

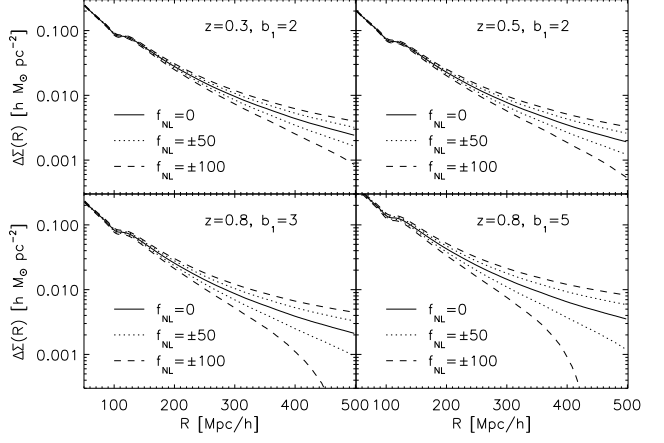


FIG. 4: Imprints of the local-type primordial non-Gaussianity in the galaxy-galaxy lensing, $\Delta\Sigma(R)$, for the same populations of lens galaxies as in Fig. 3. The solid, dashed, and dotted lines show $f_{\text{NL}} = 0, \pm 50$, and ± 100 , respectively.

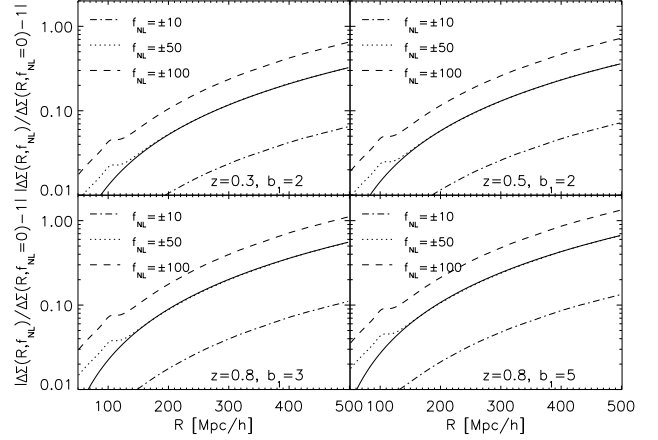


FIG. 5: Fractional differences between $\Delta\Sigma(R)$ from non-Gaussian initial conditions and the Gaussian initial condition, $|\Delta\Sigma(R; f_{\text{NL}})/\Delta\Sigma(R; f_{\text{NL}} = 0) - 1|$, calculated from the curves shown in Fig. 4. The dot-dashed, dashed, and dotted lines show $f_{\text{NL}} = \pm 10, \pm 50$, and ± 100 , respectively, while the thin solid line shows $\propto R^2$ with an arbitrary normalization.

Fig. 3 shows, for the Gaussian initial condition ($f_{\text{NL}} = 0$), $\Delta\Sigma(R, z_L)$ from $R = 50$ to $200 h^{-1} \text{ Mpc}$. We have chosen the bias parameters and lens redshifts to represent the existing data sets as well as the future ones: $b_1 = 2$ at $z_L = 0.3$ (similar to the observed values from SDSS LRGs [53], top-left), $b_1 = 2$ at $z_L = 0.5$ (higher- z LRGs [54], top-right), $b_1 = 2$ at $z_L = 0.8$ (galaxies that can be observed by LSST, [55], bottom-left), and $b_1 = 5$ at $z_L = 0.8$ (clusters of galaxies that can be observed by LSST, bottom-right). While LSST is an imaging survey, we assume that we can obtain spectroscopic redshifts of some ($\sim 10^6$) lens galaxies by follow-up observations. It is also straightforward to extend our analysis to lenses selected by photometric redshifts.

At $R \sim 110 h^{-1}$ Mpc we see a clear “shoulder” due to the baryonic feature in the linear matter power spectrum (often called Baryon Acoustic Oscillations; BAO). The sound horizon at the drag epoch (which is more relevant to the matter power spectrum than the photon decoupling epoch for the CMB power spectrum) calculated from the cosmological model that we use, the “WMAP+BAO+SN ML” parameters in Table 1 of [2], is $106.9 h^{-1}$ Mpc, as shown as the vertical line in this figure. The magnitude of $\Delta\Sigma$ on this scale is $\sim 0.1 h M_\odot \text{ pc}^{-2}$. Assuming a range of Σ_c from future surveys, $\Sigma_c \sim 1000 - 4000 h M_\odot \text{ pc}^{-2}$ (see Fig. 2), this value corresponds to the mean tangential shear of order 2.5×10^{-5} to 10^{-4} . Is this observable?

For comparison, Sheldon et al. [48] measured $\Delta\Sigma(R) \sim 0.5 h M_\odot \text{ pc}^{-2}$ at $R \sim 30 h^{-1}$ Mpc from clusters of galaxies in the SDSS main sample. The mean lens redshift for these data is $z_L \sim 0.2$, which would give $\Sigma_c \sim 5000 h M_\odot \text{ pc}^{-2}$ (see Fig. 2 for $z_L = 0.2$ and $z_S \sim 0.4$); thus, the magnitude of the mean tangential shear that they were able to measure is of order 10^{-4} , which is only ~ 1 to 4 times larger than the magnitude of the signal expected from the BAO. Therefore, detecting the BAO signature in $\Delta\Sigma(R)$ should be quite feasible with the future observations. We shall give a more quantitative discussion on the detectability of BAO from the galaxy-galaxy lensing effect in Sec IID.

How about f_{NL} ? As expected, the effect of f_{NL} is enhanced on very large scales, i.e., hundreds of Mpc (see Fig. 4). For $f_{\text{NL}} = \pm 50$, $\Delta\Sigma(R)$ is modified by 10–20% at $R \sim 300 h^{-1}$ Mpc (depending on b_1 and z_L ; see Fig. 5). The modification grows rapidly toward larger scales, in proportion to R^2 . On such a large scale ($R \sim 300 h^{-1}$ Mpc), the galaxy-galaxy lensing signal is on the order of $\Delta\Sigma \sim 0.01 h M_\odot \text{ pc}^{-2}$, and thus we need to measure the mean tangential shear down to the level of $\bar{\gamma}_t^h \sim 2.5 \times 10^{-6}$ to 10^{-5} , i.e., 10–40 times smaller than the level of sensitivity achieved by the current observations. Can we observe such a small shear?

C. Covariance matrix of the mean tangential shear

In order to study the feasibility of measuring the tangential shear of order 10^{-6} , we compute the covariance matrix of the mean tangential shears averaged over N_L lens galaxies. As derived in Appendix B, the covariance matrix of the mean tangential shear is

$$\begin{aligned} & \langle \bar{\gamma}_t^h(\theta) \bar{\gamma}_t^h(\theta') \rangle - \langle \bar{\gamma}_t^h(\theta) \rangle \langle \bar{\gamma}_t^h(\theta') \rangle \\ &= \frac{1}{4\pi f_{\text{sky}}} \int \frac{ldl}{2\pi} J_2(l\theta) J_2(l\theta') \\ & \times \left[(C_l^{h\kappa})^2 + \left(C_l^h + \frac{1}{n_L} \right) \left(C_l^\kappa + \frac{\sigma_\gamma^2}{n_S} \right) \right]. \end{aligned} \quad (18)$$

This expression includes the cosmic variance, the shot noise of lens halos, as well as the shape noise σ_γ . As

far as we know this formula has not been derived before. Note that we have assumed a single source and lens redshift. For multiple source and lens redshifts, the covariance matrix needs to be suitably generalized.

Here, C_l^h and C_l^κ are the angular power spectra of the lens halos (galaxies or cluster of galaxies) and κ , respectively, and n_L and n_S are the number densities of the lens halos and the lensed (source) galaxies, respectively. These angular power spectra, $C_l^{h\kappa}$, C_l^h , C_l^κ , will be related to the corresponding three-dimensional power spectrum, $P(k)$, in Sec III C.

In the limit that the cosmic variance is unimportant, we recover the usual expression used in the literature:

$$\langle \bar{\gamma}_t^h(\theta) \bar{\gamma}_t^h(\theta') \rangle - \langle \bar{\gamma}_t^h(\theta) \rangle \langle \bar{\gamma}_t^h(\theta') \rangle = \frac{\sigma_\gamma^2}{N_L} \frac{\delta_D(\theta - \theta')}{2\pi\theta n_S}, \quad (19)$$

where $N_L = 4\pi f_{\text{sky}} n_L$ is the total number of lens halos available in the data. In this limit the errors in different radial bins are uncorrelated, and they are simply given by the shape noise, σ_γ , reduced by the square-root of the number of source galaxies available within each radial bin and the total number of lens halos that we can use for averaging the mean tangential shear. In particular, at each bin with a width $\Delta\theta$, we find the variance of

$$\text{Var}[\bar{\gamma}_t^h(\theta)] = \frac{\sigma_\gamma^2}{2\pi\theta(\Delta\theta)n_S N_L}, \quad (20)$$

in the absence of the cosmic variance.

When would the cosmic variance become important? There is the maximum surface number density of sources, $n_{S,\text{max}} = \sigma_\gamma^2 / C_l^\kappa$, above which the shape noise becomes irrelevant. This gives the maximum number of sources within a given radial bin of a width $\Delta\theta$ ($\ll \theta$) above which the shape noise becomes irrelevant:

$$N_{S,\text{max}} = 2\pi\theta(\Delta\theta)n_{S,\text{max}} = (l\theta)^2 \left(\frac{\Delta\theta}{\theta} \right) \frac{\sigma_\gamma^2}{l^2 C_l^\kappa / (2\pi)}. \quad (21)$$

For $l\theta = \pi$ (the usual relation between l and θ) and $\sigma_\gamma \simeq 0.3$ (realistic shape noise), we find

$$N_{S,\text{max}} \simeq \left(\frac{\Delta\theta}{\theta} \right) \frac{1}{l^2 C_l^\kappa / (2\pi)}. \quad (22)$$

At $l \sim 100$, $l^2 C_l^\kappa / (2\pi) \sim 10^{-5}$ [50]; thus, we do not gain sensitivity any further by having more than, say, 10^4 galaxies (for $\Delta\theta/\theta = 0.1$) within a single radial bin.

Alternatively, one can define the minimum multipole, l_{min} , below which the cosmic variance term dominates:

$$l_{\text{min}} = \sqrt{\frac{2\pi n_S}{\sigma_\gamma^2} \frac{l^2 C_l^\kappa}{2\pi}}. \quad (23)$$

For LSST, we expect to have the surface density of sources on the order of $n_S = 30 \text{ arcmin}^{-2} = 3.5 \times 10^8 \text{ sr}^{-1}$. For $\sigma_\gamma = 0.3$, we find $l_{\text{min}}(\text{LSST}) \sim 1.6 \times$

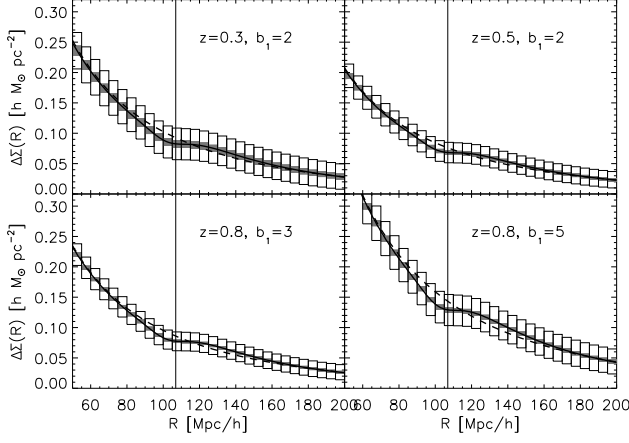


FIG. 6: Same as Fig. 3, but with the expected $1\text{-}\sigma$ uncertainties for full-sky lens surveys and a single lens redshift. Adjacent bins are highly correlated, with the correlation coefficients shown in Fig. 7. The open (filled) boxes show the binned uncertainties with (without) the cosmic variance term due to the cosmic shear field included. See Eq. (28) and (29) for the formulae giving open and filled boxes, respectively. We use the radial bin of size $\Delta R = 5 h^{-1}$ Mpc. For comparison, we also show $\Delta\Sigma(R)$ computed from the smooth power spectrum without the baryonic feature [56] (dashed lines). Note that the uncertainties are calculated for a single lens redshift slice, and thus they will go down as we add more lens redshift slices.

$10^5 \sqrt{l^2 C_l^\kappa / (2\pi)}$. At $l \lesssim 10^3$, $l^2 C_l^\kappa / (2\pi) \lesssim 10^{-4}$ [50]; thus, at $l \lesssim 10^3$ the cosmic variance term dominates.

In the limit that the covariance matrix is dominated by the cosmic variance terms, we have

$$\begin{aligned} & \langle \bar{\gamma}_t^h(\theta) \bar{\gamma}_t^h(\theta') \rangle - \langle \bar{\gamma}_t^h(\theta) \rangle \langle \bar{\gamma}_t^h(\theta') \rangle \\ &= \frac{1}{4\pi f_{\text{sky}}} \int \frac{ldl}{2\pi} J_2(l\theta) J_2(l\theta') C_l^h C_l^\kappa (1 + r_l^2), \end{aligned}$$

where $r_l \equiv C_l^{h\kappa} / \sqrt{C_l^\kappa C_l^h}$ is the cross-correlation coefficient. The variance at a given radial bin is

$$\begin{aligned} & \text{Var}[\bar{\gamma}_t^h(\theta)] \\ &= \frac{1}{4\pi f_{\text{sky}}} \int \frac{ldl}{2\pi} [J_2(l\theta)]^2 C_l^h C_l^\kappa (1 + r_l^2). \end{aligned} \quad (24)$$

D. Detectability of the mean tangential shear

In this section, we shall calculate the expected uncertainties in radially binned measurements of the mean tangential shear.

The mean tangential shear averaged within the i -th bin, $\langle \bar{\gamma}_t^h \rangle(\theta_i)$, i.e., the mean tangential shear averaged

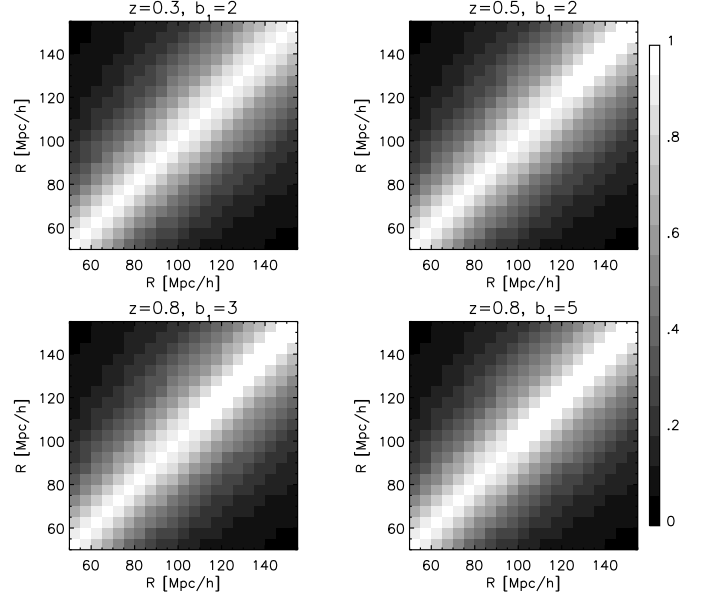


FIG. 7: The cross-correlation-coefficient matrix, $r_{ij} \equiv C_{ij} / \sqrt{C_{ii} C_{jj}}$, where C_{ij} is the covariance matrix given in Eq. (27), for a radial bin of $\Delta R = 5 h^{-1}$ Mpc. We show r_{ij} for the same populations of lens galaxies as shown in Fig. 3 and 6. We use the same number of source galaxies and the same shape noise as in Fig. 6. The neighboring bins are highly correlated for $\Delta R < 10 h^{-1}$ Mpc.

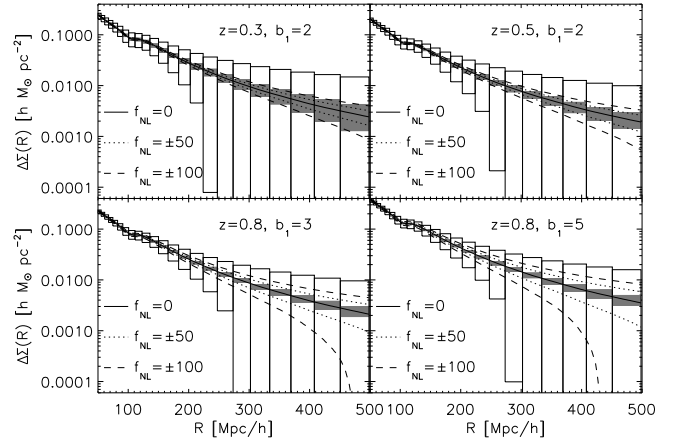


FIG. 8: Same as Fig. 4, but with the expected $1\text{-}\sigma$ uncertainties for full-sky lens surveys and a single lens redshift. Adjacent bins are highly correlated. The open (filled) boxes show the binned uncertainties with (without) the cosmic variance term due to the cosmic shear field included. See Eq. (28) and (29) for the formulae giving open and filled boxes, respectively. We use logarithmic bins with $\Delta R = R/10$. Note that the uncertainties are calculated for a single lens redshift slice, and thus they will go down as we add more lens redshift slices.

within an annulus between $\theta_{i,\min}$ and $\theta_{i,\max}$, is given by

$$\begin{aligned}\langle \hat{\gamma}_t^h \rangle(\theta_i) &= \frac{2\pi}{A(\theta_i)} \int_{\theta_{i,\min}}^{\theta_{i,\max}} \theta d\theta \langle \hat{\gamma}_t^h \rangle(\theta) \\ &\equiv \int \frac{ldl}{2\pi} C_l^{h\kappa} \hat{J}_2(l\theta_i),\end{aligned}\quad (25)$$

where $A(\theta_i) = \pi(\theta_{i,\max}^2 - \theta_{i,\min}^2)$ is the area of the annulus, and

$$\hat{J}_2(l\theta_i) = \frac{2\pi}{A(\theta_i)} \int_{\theta_{i,\min}}^{\theta_{i,\max}} \theta d\theta J_2(l\theta), \quad (26)$$

is the Bessel function averaged within a bin.

Similarly, the covariance matrix of the binned mean tangential shears is given by

$$\begin{aligned}C_{ij} &\equiv \langle \hat{\gamma}_t^h(\theta_i) \hat{\gamma}_t^h(\theta_j) \rangle - \langle \hat{\gamma}_t^h(\theta_i) \rangle \langle \hat{\gamma}_t^h(\theta_j) \rangle \\ &= \frac{1}{4\pi f_{\text{sky}}} \int \frac{ldl}{2\pi} \hat{J}_2(l\theta_i) \hat{J}_2(l\theta_j) \\ &\quad \times \left[(C_l^{h\kappa})^2 + \left(C_l^h + \frac{1}{n_L} \right) \left(C_l^\kappa + \frac{\sigma_\gamma^2}{n_S} \right) \right]\end{aligned}\quad (27)$$

This matrix contains the full information regarding the statistical errors of the binned measurements of the mean tangential shear, which includes the cosmic variance errors due to the cosmic shear (C_l^κ), clustering of lens galaxies (C_l^h) and their correlations ($C_l^{h\kappa}$), the finite number density of lenses, and the noise in intrinsic shapes of source galaxies.

The variance at a given radial bin is

$$\begin{aligned}\text{Var}[\hat{\gamma}_t^h(\theta_i)] &= \frac{1}{4\pi f_{\text{sky}}} \int \frac{ldl}{2\pi} [\hat{J}_2(l\theta_i)]^2 \\ &\quad \times \left[(C_l^{h\kappa})^2 + \left(C_l^h + \frac{1}{n_L} \right) \left(C_l^\kappa + \frac{\sigma_\gamma^2}{n_S} \right) \right]\end{aligned}\quad (28)$$

In the analysis of the galaxy-galaxy lensing effects in the literature, the cosmic variance due to cosmic shear is usually ignored:

$$\begin{aligned}\text{Var}[\hat{\gamma}_t^h(\theta_i)] \Big|_{\kappa=0} &= \frac{1}{4\pi f_{\text{sky}}} \int \frac{ldl}{2\pi} [\hat{J}_2(l\theta_i)]^2 \\ &\quad \times \left[\left(C_l^h + \frac{1}{n_L} \right) \frac{\sigma_\gamma^2}{n_S} \right].\end{aligned}\quad (29)$$

This is probably a reasonable approximation for the current measurements at $R \lesssim 30 h^{-1}$ Mpc; however, on larger scales which will be probed by the next-generation lens surveys, the cosmic variance due to cosmic shear must be included, as we show in Fig. 6.

For estimating the expected uncertainties, we assume a million lens galaxies with very narrow (delta-function like) redshift distribution centered at z_L ($N_L = 10^6$) over the full sky, $f_{\text{sky}} = 1$. We also assume $\sigma_\gamma = 0.3$, and

$n_S = 3.5 \times 10^8 \text{ sr}^{-1}$. As the covariance matrix is dominated by the cosmic variance terms, the size of open boxes is insensitive to the exact values of N_L , σ_γ , or n_S . (See Sec. III C.) First, we calculate the binned uncertainties in the region close to the baryonic feature, $R \sim 110 h^{-1}$ Mpc. In Fig. 6, the open boxes show the full uncertainties including the cosmic variance due to cosmic shear (Eq. (28)), while the filled boxes show the uncertainties without the cosmic shear term (Eq. (29)). The latter is clearly negligible compared to the former on large scales, $R \gtrsim 50 h^{-1}$ Mpc.

Can we distinguish $\Delta\Sigma(R)$ with and without the baryonic feature? Without baryons, we do not see any features in $\Delta\Sigma(R)$; see dashed lines in Fig. 6 which are calculated from the smooth linear power spectrum without the baryonic feature [56]. To see if we can detect this feature in $\Delta\Sigma(R)$, we estimate the χ^2 difference between $\Delta\Sigma(R)$ with and without the baryonic feature:

$$\Delta\chi^2 \equiv \sum_{i,j} (\Delta\Sigma_i - \Delta\Sigma_{i,\text{nw}}) C_{ij}^{-1} (\Delta\Sigma_j - \Delta\Sigma_{j,\text{nw}}),$$

where $\Delta\Sigma_i$ is the mean tangential shear of i -th bin, $\Delta\Sigma_{\text{nw}}$ is $\Delta\Sigma$ without the baryonic feature, and C_{ij}^{-1} is the inverse of the binned covariance matrix (Eq. 27). Using only a single lens redshift slice, we find $\Delta\chi^2 = 0.85$ ($z_L = 0.3$, $b = 2$), 1.07 ($z_L = 0.5$, $b = 2$), 1.32 ($z_L = 0.8$, $b = 3$), and 1.34 ($z_L = 0.8$, $b = 5$). For example, if we add up all these measurements at different slices ($z_L = 0.3$, 0.5 and 0.8), significance of detection of the baryonic feature is $\Delta\chi^2 = 3.2$, i.e., 93% C.L. As we expect to have many more lens redshift slices from the future lens surveys, detection and measurement of the baryonic feature in $\Delta\Sigma$ are quite feasible. For multiple lens slices the gain in the signal-to-noise ratio will be approximately $\sqrt{N_{\text{lens}}}$; thus, for 10 lens slices the errors would be a factor of 3 smaller. At best we can expect ~ 25 slices, which gives a factor of 5 reduction in errors.

What about f_{NL} ? We show the expected 1- σ uncertainties for the mean tangential shears, $\Delta\Sigma(R)$, on larger scales in Fig. 8. For this figure we use logarithmic bins with the radial size of $\Delta R/R = 0.1$. We find that $\Delta\Sigma(R)$ on $R \simeq 250 h^{-1}$ Mpc is detectable, even from a single lens redshift slice. This is remarkable; however, the predicted uncertainties are too large for us to distinguish between $f_{\text{NL}} = 0$ and $f_{\text{NL}} = 100$ using a single lens redshift slice. In order to obtain a tight limit on f_{NL} , we would need to include many lens redshift slices.

Note that the uncertainty at a given R is larger for a smaller lens redshift. This is because a given R corresponds to a larger angular size for a lower lens redshift, making the cosmic variance contribution greater.

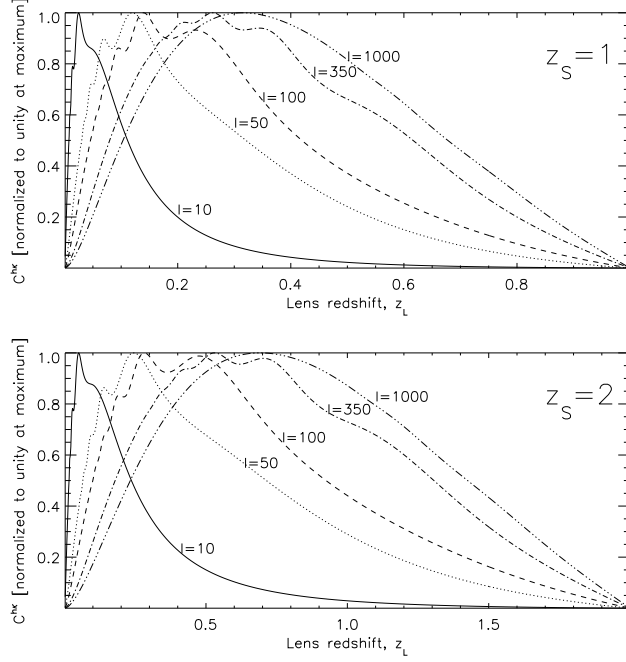


FIG. 9: Angular power spectrum of the galaxy-convergence cross correlation, $C_l^{h\kappa}$, at various multipoles as a function of the lens redshift, z_L , for two effective source redshifts, $z_s = 1$ (top) and 2 (bottom). We have divided $C_l^{h\kappa}$ by its maximum value. The solid, dotted, dashed, dot-dashed, and triple-dot-dashed lines show $l = 10, 50, 100, 350$, and 1000 , respectively.

III. HARMONIC SPACE APPROACH

A. Formula

The mean tangential shear, $\langle \bar{\gamma}_t^h \rangle$ or $\Delta\Sigma$, is currently widely used for measuring the halo-shear cross correlation, as this method is easy to implement and is less sensitive to systematic errors.

In this section, we shall study the effects of f_{NL} on the equivalent quantity in harmonic space: the halo-convergence cross power spectrum, $C_l^{h\kappa}$. The mean tangential shear is related to $C_l^{h\kappa}$ by the 2-dimensional Fourier integral given in Eq. (11).

The convergence field, $\kappa(\mathbf{n})$, is the matter density fluctuations projected on the sky:

$$\kappa(\mathbf{n}) = \int_0^\infty dz W_\kappa(z) \delta_m[d_A(0; z) \mathbf{n}, z], \quad (30)$$

where $\delta_m(\mathbf{r}, z) \equiv \rho_m(\mathbf{r}, z)/\bar{\rho}_m(z) - 1$, and $W_\kappa(z)$ is a lens kernel which describes the efficiency of lensing for a given redshift distribution of sources, $p(z_S)$:

$$W_\kappa(z) = \frac{\rho_0}{\Sigma_c(z; z_S) H(z)}, \quad (31)$$

where the critical density, Σ_c , is defined in Eq. (16).

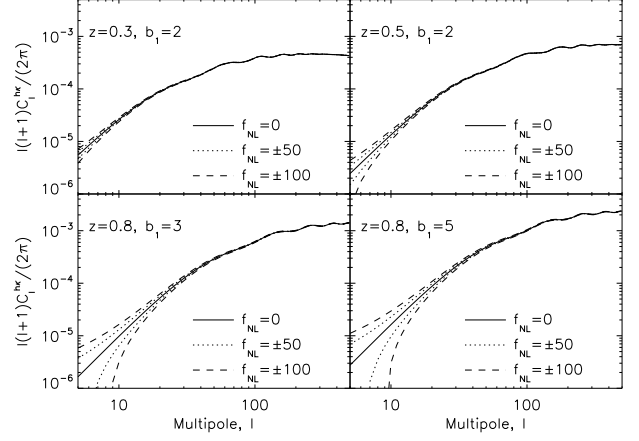


FIG. 10: Imprints of the local-type primordial non-Gaussianity in the galaxy-convergence cross power spectrum, $l(l+1)C_l^{h\kappa}/(2\pi)$, for the same populations of lens galaxies as in Fig. 3. The solid, dashed, and dotted lines show $f_{NL} = 0, \pm 50$, and ± 100 , respectively.

Again using Limber's approximation (whose validity and limitation are studied in Appendix C), we find the relation between the angular cross-correlation power spectrum of the convergence field and the halo density at a given lens redshift z_L , $C_l^{h\kappa}(z_L)$, and the halo-mass cross-correlation power spectrum at the same redshift, $P_{hm}(k, z_L)$, as

$$\begin{aligned} C_l^{h\kappa}(z_L) &= \frac{\rho_0}{\Sigma_c(z_L; z_S) d_A^2(0; z_L)} P_{hm} \left[k = \frac{l+1/2}{d_A(0; z_L)}, z_L \right] \\ &= \frac{4\pi G \rho_0}{c^2} (1+z_L) \frac{d_A(z_L; z_S)}{d_A(0; z_L) d_A(0; z_S)} \\ &\quad \times P_{hm} \left[k = \frac{l+1/2}{d_A(0; z_L)}, z_L \right]. \end{aligned} \quad (32)$$

Fig. 9 shows $C_l^{h\kappa}(z_L)$ for the Gaussian density field as a function of lens redshifts, z_L . The convergence fields at low (high) multipoles are better correlated with low- z (high- z) galaxies. This is due to the shape of the matter power spectrum: on very large scales (i.e., low l), the matter power spectrum is given by the initial power spectrum, $P_{hm}(k) \propto k$, and thus we get $1/d_A(0; z_L)$ from $P_{hm}[k = l/d_A(0; z_L)]$. This gives a larger weight to low- z galaxies. On smaller scales where $P_{hm}(k) \propto k^{n_{\text{eff}}}$ with $n_{\text{eff}} \simeq -3$, we get positive powers of $d_A(0; z_L)$ from $P_{hm}[k = l/d_A(0; z_L)]$, which gives a larger weight to high- z galaxies.

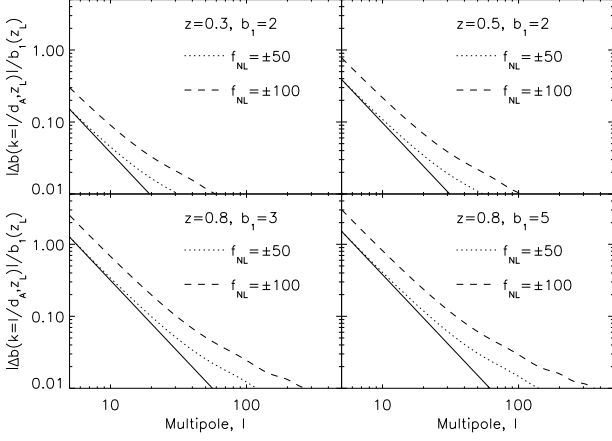


FIG. 11: Fractional differences between $C_l^{h\kappa}$ from non-Gaussian initial conditions and the Gaussian initial condition, calculated from the curves shown in Fig. 10. These differences are equal to $|\Delta b(l = k/d_A, z_L)|/b_1(z_L)$. The dashed and dotted lines show $f_{NL} = \pm 50$ and ± 100 , respectively, while the thin solid lines show l^{-2} with an arbitrary normalization.

B. Result

We can now calculate $C_l^{h\kappa}$ for various values of f_{NL} . We use

$$C_l^{h\kappa}(z_L) = \frac{4\pi G\rho_0}{c^2}(1+z_L)\frac{d_A(z_L; z_S)}{d_A(0; z_L)d_A(0; z_S)} \times \left[b_1(z_L) + \Delta b\left(k = \frac{l+1/2}{d_A(0; z_L)}, z_L\right) \right] \times P_m\left[k = \frac{l+1/2}{d_A(0; z_L)}, z_L\right], \quad (33)$$

where the scale-dependent bias, $\Delta b(k, z)$, is given by Eq. (3).

Figure 10 shows $C_l^{h\kappa}(z_L)$ for $f_{NL} = \pm 50$ and ± 100 for populations of galaxies that we have considered in the previous sections. For each lens redshift, we calculate the “effective” source redshift by requiring that the angular diameter distance to the source redshift is twice as large as that to the lens redshift, i.e., $d_A(0; z_S) = 2d_A(0; z_L)$. With this requirement, the source redshifts are $z_s = 0.65, 1.19$, and 2.25 for $z_L = 0.3, 0.5$, and 0.8 , respectively.

Figure 11 shows the fractional differences between non-Gaussian predictions and the Gaussian prediction ($f_{NL} = 0$), which are simply equal to $\Delta b(k, z_L)/b_1(z_L)$ where $k = l/d_A(0; z_L)$. As expected from the form of the scale-dependent bias, the difference grows toward small multipoles as roughly $1/l^2$. While lower redshift populations do not show more than 10% difference at $l \geq 10$ for $f_{NL} = \pm 50$, a higher- z population of lens galaxies or clusters of galaxies at $z_L = 0.8$ show the differences at the level of $\sim 10\%$ at $l \geq 20$ and $\sim 30\%$ at $l \sim 10$. Are these effects detectable?

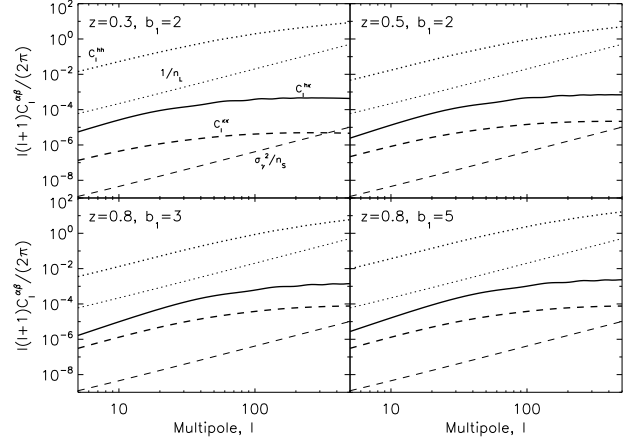


FIG. 12: Angular power spectra of the galaxy-galaxy correlation, C_l^h (thick dotted lines), the galaxy-convergence cross-correlation, $C_l^{h\kappa}$ (thick solid lines), and the convergence-convergence correlation, C_l^κ (thick dashed lines) for the Gaussian initial condition ($f_{NL} = 0$). The four panels show the same populations of galaxies and clusters of galaxies as in Fig. 10. We also show the galaxy shot noise, $1/n_L$ (thin dotted lines) as well as the source shape noise, σ_γ^2/n_S (thin dashed lines), for $N_L = 10^6$, $\sigma_\gamma = 0.3$, and $n_S = 3.5 \times 10^8 \text{ sr}^{-1}$. We find $1/n_L \ll C_l^h$ and $\sigma_\gamma^2/n_S \ll C_l^\kappa$ for $l \lesssim 100$.

C. Covariance matrix of the galaxy-convergence cross power spectrum

The covariance matrix of the galaxy-convergence cross-correlation power spectrum is given by

$$\begin{aligned} & \langle C_l^{h\kappa} C_{l'}^{h\kappa} \rangle - \langle C_l^{h\kappa} \rangle \langle C_{l'}^{h\kappa} \rangle \\ &= \frac{\delta_{ll'}}{(2l+1)f_{\text{sky}}} \left[(C_l^{h\kappa})^2 + \left(C_l^h + \frac{1}{n_L} \right) \left(C_l^\kappa + \frac{\sigma_\gamma^2}{n_S} \right) \right] \end{aligned} \quad (34)$$

where $\delta_{ll'}$ is Kronecker’s delta symbol showing that the angular power spectra at different multipoles are uncorrelated. Again, C_l^h and C_l^κ are the angular power spectra of the lens halos (galaxies or cluster of galaxies) and κ , respectively, and n_L and n_S are the number densities of the lens halos and the lensed (source) galaxies, respectively.

We calculate C_l^κ by using Limber’s approximation as

$$C_l^\kappa = \int_0^{z_S} dz \frac{\rho_0^2}{\Sigma_c^2(z; z_S)} \frac{P_m\left[k = \frac{l+1/2}{d_A(0; z)}; z\right]}{H(z)d_A^2(0; z)}. \quad (35)$$

However, we cannot use Limber’s approximation for C_l^h unless one considers lens redshift slices that are broad. As we are assuming a thin lens redshift slice throughout this paper, we must not use Limber’s approximation, but evaluate the exact integral relation:

$$C_l^h = \frac{2}{\pi} \int dk k^2 P_g(k, z_L) j_l^2[kd_A(z_L)], \quad (36)$$

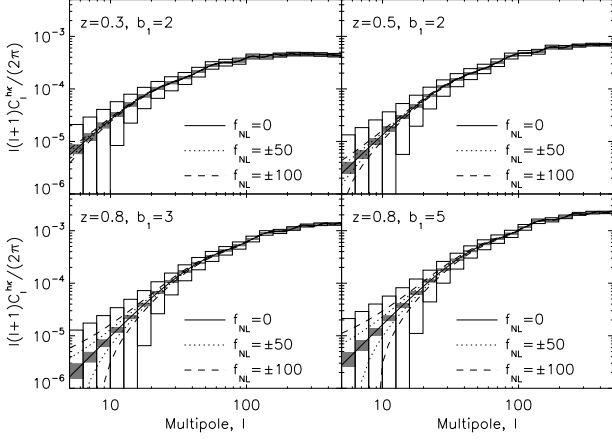


FIG. 13: Same as Fig. 10, with the expected $1\text{-}\sigma$ uncertainties for full-sky lens surveys and a single lens redshift. Adjacent bins are uncorrelated. The open (filled) boxes show the binned uncertainties with (without) the cosmic variance term due to the cosmic shear field included. We used Eq. (34) for the open boxes, and Eq. (34) with $C_l^{h\kappa} = 0 = C_l^\kappa$ for the filled boxes. We use logarithmic bins of $\Delta l = 0.23l$. Note that the uncertainties are calculated for a single lens redshift slice, and thus they will go down as we add more lens redshift slices.

where j_l is the spherical Bessel function, and $P_g(k, z)$ is the linear galaxy power spectrum: $P_g(k) = b_1^2 P_m(k)$.

Fig. 12 shows the galaxy-galaxy, galaxy-convergence, and convergence-convergence angular power spectra for Gaussian ($f_{\text{NL}} = 0$) initial conditions. We also show the shot noise of the galaxy angular power spectrum, $1/n_L$, and the shape noise of the convergence power spectrum, σ_γ^2/n_S , with the following representative values: $N_L = 4\pi n_L = 10^6$, $n_S = 3.5 \times 10^8 \text{ sr}^{-1}$, and $\sigma_\gamma = 0.3$. We find $1/n_L \ll C_l^h$ and $\sigma_\gamma^2/n_S \ll C_l^\kappa$ for the multipoles that we are interested in, i.e., $l \lesssim 100$, and thus we conclude that the uncertainties are totally dominated by the cosmic variance terms. In other words, the size of the uncertainties are insensitive to the exact choices of N_L , σ_γ , or n_S .

We also find that the values of cross correlation coefficients, $r_l \equiv C_l^{h\kappa} / \sqrt{C_l^h C_l^\kappa}$, are small (of order 10–20%): the maximum values are 0.19, 0.15, and 0.13 for $z_L = 0.3$, 0.5, and 0.8, respectively. This implies that one may ignore the contribution of $C_l^{h\kappa}$ to the covariance matrix, approximating the variance of $C_l^{h\kappa}$ of a single lens redshift slice for a multipole bin of size Δl as:

$$\text{Var}(C_l^{h\kappa}) = \frac{C_l^h C_l^\kappa}{(2l+1)\Delta l f_{\text{sky}}}. \quad (37)$$

Therefore, we should be able to measure the galaxy-convergence cross-power spectrum with $C_l^{h\kappa} / \sqrt{\text{Var}(C_l^{h\kappa})} \gtrsim 1$ when the multipoles satisfy

$$l \gtrsim l_{\min} \equiv \frac{1}{r_l \sqrt{2(\Delta l/l) f_{\text{sky}}}}. \quad (38)$$

For the galaxy-convergence power spectra in Fig. 10 with the full sky coverage ($f_{\text{sky}} = 1$) and $\Delta l/l = 0.23$, we find $l_{\min} = 9.0, 12.1$, and 15.7 for $z_L = 0.3$ ($z_S = 0.65$), 0.5 (1.19), and 0.8 (2.25), respectively.

Similarly, we can estimate the maximum radius below which we can measure the mean tangential shear, $\Delta\Sigma(R)$, as

$$R_{\max} \simeq \frac{\pi d_A(0; z_L)}{l_{\min}}. \quad (39)$$

For example, with $\Delta R/R = \Delta l/l = 0.1$, we get $R_{\max} \simeq 215, 260$, and $300 h^{-1} \text{ Mpc}$ for $z_L = 0.3, 0.5$ and 0.8 , respectively. These values do give the radii at which the signal-to-noise ratios are roughly unity in Fig. 8.

Fig. 13 shows the expected $1\text{-}\sigma$ uncertainties of $C_l^{h\kappa}$ for several populations of lens galaxies. We find that the cosmic variance completely dominates the uncertainties on large scales (low l) where the non-Gaussian effects are the largest. Again, while we find that it would be difficult to measure f_{NL} from a *single lens redshift slice*, combining many redshift slices should help us measure f_{NL} , especially when we can use many slices at moderately high redshifts.

IV. HALO-MASS CORRELATION FROM GALAXY-CMB LENSING

A. Formula

Instead of using the background galaxies for measuring the cosmic shear field due to the intervening mass, one can use the CMB as the background light and measure the shear field of the *CMB lensing* due to the intervening mass between us and the photon decoupling epoch at $z_* \simeq 1089$. See [57] for a review on the CMB lensing.

The lensing effect makes CMB anisotropies (both temperature and polarization) non-Gaussian by producing a non-vanishing connected four-point function, although it does not produce any non-vanishing three-point function. One can use this property to reconstruct the lensing potential field, hence the projected mass-density field between us and z_* , from the four-point function of CMB [58, 59, 60].

By cross-correlating the halo over-density field, δ_h , at some redshift z_L (measured from spectroscopic observations) and the κ field reconstructed from the CMB lensing, one can measure the halo-convergence angular power spectrum, $C_l^{h\kappa}$.

The angular power spectrum of the galaxy-CMB lensing cross correlation is merely a special case of the galaxy-convergence cross correlation that we have studied in the previous section: all we need to do is to set the source redshift, z_S , to be the redshift of the photon decoupling epoch, $z_* \simeq 1089$, i.e., $z_S = z_*$. Note that for a flat universe $d_A(z_L; z_*) = d_A(0; z_*) - d_A(0; z_L)$ where $d_A(0; z_*) = 9.83 h^{-1} \text{ Gpc}$.

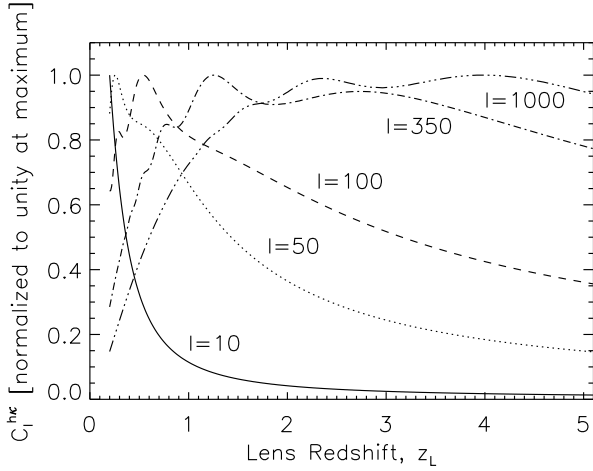


FIG. 14: Angular power spectrum of the galaxy-CMB lensing, $C_l^{h\kappa}$, at various multipoles as a function of the lens redshift, z_L . We have divided $C_l^{h\kappa}$ by its maximum value. The solid, dotted, dashed, dot-dashed, and triple-dot-dashed lines show $l = 10, 50, 100, 350$, and 1000 , respectively.

Figure 14 shows that the CMB lensing at low (high) multipoles are better correlated with low- z (high- z) galaxies. This is due to the shape of the matter power spectrum, as we have explained in the previous section. Note that $C_l^{h\kappa}$ of the CMB lensing for a given multipole decreases more slowly with z_L than that of the galaxy lensing due to the geometrical factor $d_A(z_L; z_S)/d_A(0; z_S)$.

Note that CMB and galaxies at $z \lesssim 1$ are correlated also via the Integrated Sachs-Wolfe (ISW) effect [61]. We shall not include this effect in our cross-correlation calculation for the following reason. We calculate the cross-correlation signal between galaxies and the convergence field reconstructed from CMB. This reconstruction relies on the fact that lensed CMB fluctuations have non-vanishing connected four-point function. On the other hand, the linear ISW effect does not have such a particular form of four-point function induced by lensing, and thus should not contribute to the reconstructed convergence field. See [34] for the effects of f_{NL} on the galaxy-ISW cross correlation.

B. Results

We can now calculate $C_l^{h\kappa}$ for various values of f_{NL} . We use

$$C_l^{h\kappa}(z_L) = \frac{4\pi G\rho_0}{c^2}(1+z_L)\frac{d_A(z_L; z_*)}{d_A(0; z_L)d_A(0; z_*)} \times \left[b_1(z_L) + \Delta b\left(k = \frac{l}{d_A(0; z_L)}, z_L\right) \right] \times P_m\left[k = \frac{l}{d_A(0; z_L)}, z_L\right], \quad (40)$$

where the scale-dependent bias, $\Delta b(k, z)$, is given by Eq. (3).

Figure 15 shows $C_l^{h\kappa}(z_L)$ for $f_{NL} = \pm 50$ and ± 100 for populations of low- z galaxies that we have considered in the previous sections: $b_1 = 2$ at $z_L = 0.3$ (similar to SDSS LRGs, top-left), $b_1 = 2$ at $z_L = 0.5$ (higher- z LRGs, top-right), $b_1 = 2$ at $z_L = 0.8$ (galaxies that can be observed by LSST, bottom-left), and $b_1 = 5$ at $z_L = 0.8$ (clusters of galaxies that can be observed by LSST, bottom-right). The fractional differences between non-Gaussian predictions and the Gaussian prediction ($f_{NL} = 0$) are exactly the same as those shown in Fig. 11: in the limit where Limber's approximation is valid, the galaxy-convergence power spectrum and the galaxy-CMB lensing power spectrum for the same lens galaxies differ only by a constant geometrical factor of $d_A(z_L; z_*)d_A(0; z_S)/d_A(z_L; z_S)d_A(0; z_*)$. Incidentally, for our choice of the source redshifts in the previous section, $2d_A(z_L; z_*)/d_A(0; z_*) = 1.83, 1.73$, and 1.60 for $z_L = 0.3, 0.5$, and 0.8 , respectively.

Therefore, the galaxy-CMB lensing cross correlation would provide a nice cross-check for systematics of the galaxy-convergence cross correlation, and *vice versa*: after all, we are measuring the same quantity, $P_{hm}(k)$, by two different background sources, high- z galaxies and CMB.

In using high- z galaxies as sources, the galaxy-galaxy lensing measurement may be susceptible to systematic errors widely discussed in the lensing literature, namely shear calibration, coherent point spread function (PSF) anisotropy, redshift biases, magnification bias and intrinsic alignments of galaxies. Here we are particularly concerned with errors that affect galaxy-shear cross-correlations by mimicking the angular dependence of the signal due to non-zero f_{NL} . Fortunately most systematic errors that affect shear-shear correlations do not contribute to galaxy-shear cross correlations: for instance, PSF anisotropy affects background galaxy shapes but not foreground galaxy locations [62]. With standard lensing data analysis methods, it can be ensured that both the shear calibration and PSF do not contribute a scale dependence to the first order. Biases in the redshift distributions of lens and source galaxies can similarly lead to a mis-estimation of the amplitude of the signal, but not its scale dependence. Thus, to the lowest order, the measurement of f_{NL} via the scale dependence of the galaxy-galaxy lensing signal is robust to the leading systematic errors in weak lensing. But a detailed study of various sources of error is needed given the small signal we are seeking.

Another benefit of using the CMB lensing as a proxy for the intervening matter distribution is that we can probe the galaxy-matter cross correlation at high redshift to which we cannot reach with the galaxy-galaxy lensing method. It is especially useful for probing primordial non-Gaussianity, as the scale dependent bias signal is higher for higher lens redshift: $\Delta b(k, z_L) \propto 1/D(z_L)$ (see Eq. (3)). Therefore, we find that even higher- z pop-

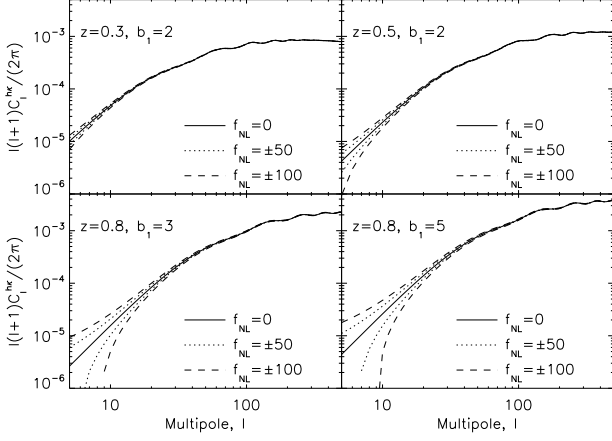


FIG. 15: Imprints of the local-type primordial non-Gaussianity in the galaxy-CMB lensing power spectrum, $l(l+1)C_l^{h\kappa}/(2\pi)$, for the same populations of lens galaxies as in Fig. 3. The solid, dashed, and dotted lines show $f_{\text{NL}} = 0$, ± 50 , and ± 100 , respectively.

ulations of galaxies give us a much better chance of detecting the effects of f_{NL} . Figure 16 shows $C_l^{h\kappa}(z_L)$ for $f_{\text{NL}} = \pm 50$ and ± 100 for populations of high- z galaxies: $b_1 = 2$ at $z_L = 2$ (top-left), $b_1 = 2.5$ at $z_L = 3$ (top-right), $b_1 = 3$ at $z_L = 4$ (bottom-left), and $b_1 = 3.5$ at $z_L = 5$ (bottom-right). The first one, a spectroscopic galaxy survey at $z_L = 2$ with $b_L = 2$, is within reach by, e.g., the Hobby-Eberly Telescope Dark Energy Experiment (HETDEX) [63, 64]. There we find, for $f_{\text{NL}} = \pm 50$, $\sim 10\%$ effect at $l \sim 40$, and a factor of two effect at $l \sim 10$ (see Fig. 17). The effects grow bigger at higher z : higher- z surveys at $z > 3$ can be done with, e.g., the concept of the Cosmic Inflation Probe (CIP)⁵. At $z_L = 4$ and 5 (with $b_1 = 3$ and 4, respectively) we find $\sim 10\%$ effect at $l \sim 100$, a factor of two effect at $l \sim 30$, and even bigger effects at $l \lesssim 30$ (see Fig. 17).

C. Covariance matrix of the galaxy-CMB lensing

The covariance matrix of the galaxy-CMB lensing is given by [65]

$$\begin{aligned} & \langle C_l^{h\kappa} C_{l'}^{h\kappa} \rangle - \langle C_l^{h\kappa} \rangle \langle C_{l'}^{h\kappa} \rangle \\ &= \frac{(C_l^{h\kappa})^2 + (C_l^h + 1/n_L)(C_l^\kappa + N_l^\kappa)}{(2l+1)f_{\text{sky}}} \delta_{ll'}, \end{aligned} \quad (41)$$

where N_l^κ is the reconstruction noise from CMB given by [58]. The covariance matrix equation here is the same as Eq. (34), except that now the shape noise of source galaxies is replaced by the reconstruction noise of CMB

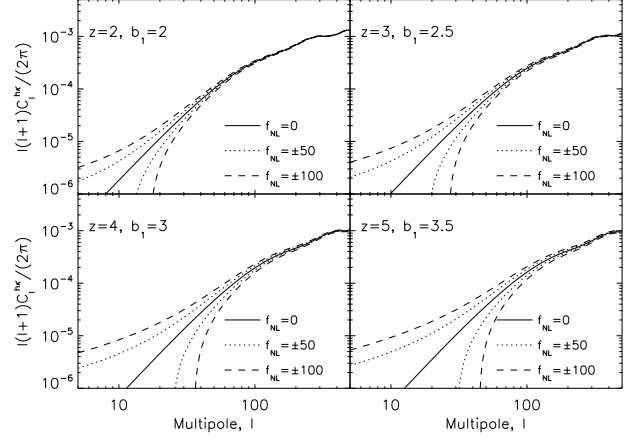


FIG. 16: Same as Fig. 15, but for high- z lens galaxies with $b_1 = 2$ at $z_L = 2$ (top-left), $b_1 = 2.5$ at $z_L = 3$ (top-right), $b_1 = 3$ at $z_L = 4$ (bottom-left), and $b_1 = 3.5$ at $z_L = 5$ (bottom-right).

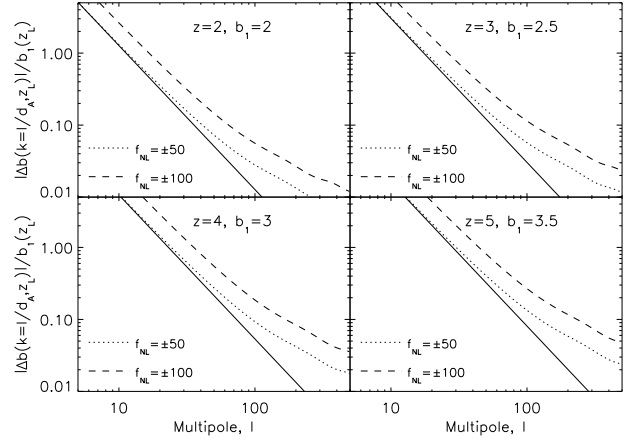


FIG. 17: Same as Fig. 11, but for high- z lens galaxies with $b_1 = 2$ at $z_L = 2$ (top-left), $b_1 = 2.5$ at $z_L = 3$ (top-right), $b_1 = 3$ at $z_L = 4$ (bottom-left), and $b_1 = 3.5$ at $z_L = 5$ (bottom-right).

lensing. In what follows, we shall assume a “nearly perfect” CMB experiment considered in Hu and Okamoto [58], whose Gaussian random detector noise is modeled as [66]

$$\begin{aligned} C_l^T \Big|_{\text{noise}} &= \left(\frac{T_{\text{CMB}}}{\Delta_T} \right)^{-2} e^{l(l+1)\sigma^2/8 \ln 2}, \\ C_l^E \Big|_{\text{noise}} &= C_l^B \Big|_{\text{noise}} = \left(\frac{T_{\text{CMB}}}{\Delta_T} \right)^{-2} e^{l(l+1)\sigma^2/8 \ln 2} \end{aligned} \quad (42)$$

where the white noise level of detectors is $\Delta_T = \Delta_P/\sqrt{2} = 1 \mu\text{K arcmin}$, and the Full-Width-at-Half-Maximum (FWHM) of the beam is $\sigma = 4'$. With these detector parameters and the cosmological parameters of the “WMAP+BAO+SN ML” parameters in Table 1 of [2], we find $N_l^\kappa \simeq 6 \times 10^{-8} \text{ sr}^{-1}$ on large scales, $l < 100$.

⁵ <http://www.cfa.harvard.edu/cip/>

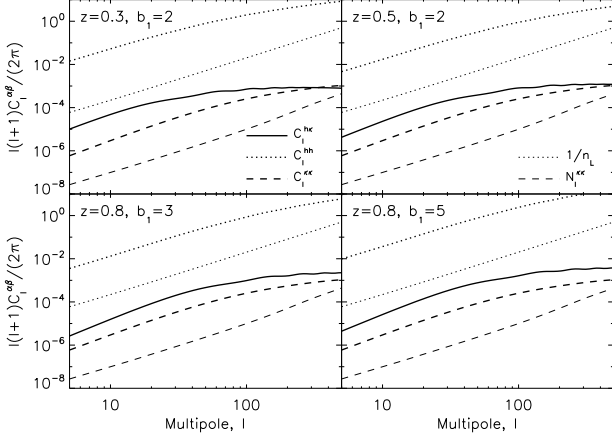


FIG. 18: Angular power spectra of the galaxy-galaxy correlation, C_l^h (thick dotted lines), the galaxy-convergence cross-correlation, $C_l^{h\kappa}$ (thick solid lines), and the convergence-convergence correlation, C_l^κ (thick dashed lines) for the Gaussian initial condition ($f_{\text{NL}} = 0$). The four panels show the same populations of galaxies and clusters of galaxies as in Fig. 15. We also show the galaxy shot noise, $1/n_L$ (thin dotted lines) as well as the lens reconstruction noise, N_l^κ (thick dashed lines), for $N_L = 10^6$ and $N_l^\kappa \simeq 6 \times 10^{-8} \text{ sr}^{-1}$ (for multipoles much smaller than that corresponds to the beam size of $4'$). We find $1/n_L \ll C_l^h$ and $N_l^\kappa \ll C_l^\kappa$ for $l \lesssim 100$.

Fig. 18 shows the galaxy-galaxy, galaxy-convergence, convergence-convergence angular power spectra for the Gaussian initial condition ($f_{\text{NL}} = 0$). This figure is qualitatively similar to Fig. 12: the galaxy-galaxy correlation is exactly the same, and the galaxy-convergence power spectrum is simply a scaled version of the corresponding curve in Fig. 12. The major difference comes from C_l^κ : as the CMB photons travel a longer path than photons from source galaxies, the convergence-convergence power spectrum is higher for the CMB lensing convergence.

On large scales ($l \lesssim 100$), the covariance matrix is dominated by the cosmic variance terms: $1/n_L \ll C_l^h$ and $N_l^\kappa \ll C_l^\kappa$. The cross correlation coefficients are small, of order 10%: the maximum values are 0.12, 0.11, and 0.10 for $z_L = 0.3, 0.5$, and 0.8 , respectively. Therefore, we can again use Eq. (37) for estimating the variance, and find l_{min} (Eq. (38)) above which we can measure the galaxy-convergence cross correlation with the signal-to-noise ratio greater than unity. For logarithmic bins of $\Delta l/l = 0.23$, we find $l_{\text{min}} = 12.2, 13.5$, and 15.8 for $z_L = 0.3, 0.5$, and 0.8 , respectively. Comparing to the results in Sec III C, l_{min} is slightly bigger, as C_l^κ (which contributes to the uncertainty) increases more rapidly than $C_l^{h\kappa}$ (the signal we are after) would as the source redshift increases from z_S to z_* .

Fig. 19 shows the expected $1\text{-}\sigma$ uncertainties of the angular power spectrum of the galaxy-CMB lensing cross correlation, on top of the predicted Gaussian/non-Gaussian signals with five different values of non-Gaussianity parameters: $f_{\text{NL}} = 0, \pm 50, \pm 100$. We also

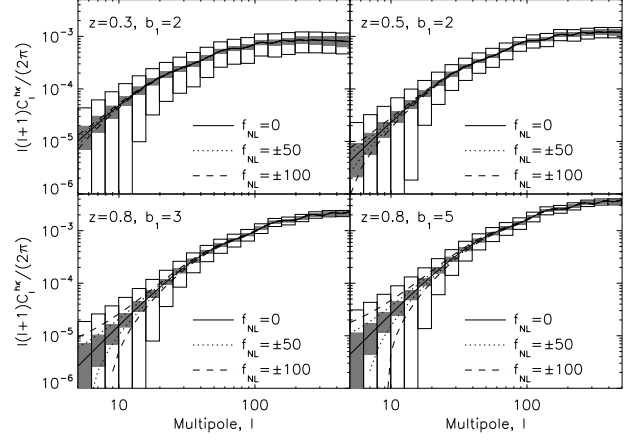


FIG. 19: Same as Fig. 15, but with $1\text{-}\sigma$ uncertainty due to the shape noise of source galaxies (filled box, Eq. (29)) and full error budget (empty box, diagonal of Eq. (27)) including the cosmic variance. We use the multipole bins of size $\Delta l = 0.23l$. For uncertainty of CMB lensing reconstruction, We assume the nearly-perfect reference experiment of Hu and Okamoto [58]: white detector noise $\Delta_T = \Delta_P/\sqrt{2} = 1 \mu\text{K arcmin}$, and FWHM of the beam $\sigma = 4'$.

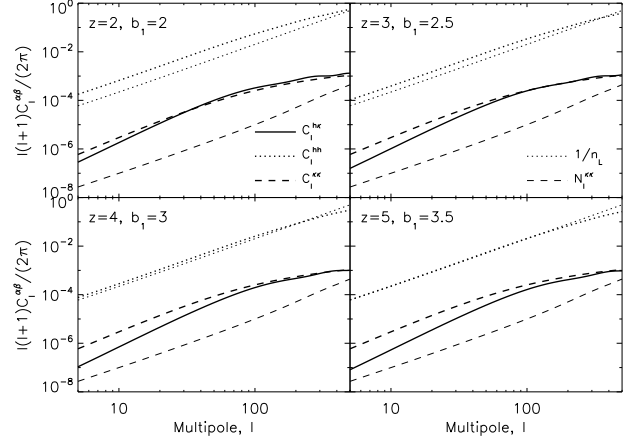


FIG. 20: Same as Fig. 18, but for the high redshift lens galaxies shown in Fig. 16. For these populations (and with $N_L = 10^6$), the shot noise is about the same as the galaxy power spectrum, i.e., $C_l^h \simeq 1/n_L$.

show the $1\text{-}\sigma$ uncertainties without the cosmic variance due to the cosmic shear. Once again, it would be difficult to measure the effects of f_{NL} from a single lens redshift, but combining many slices would help measure f_{NL} from the galaxy-CMB lensing cross correlation.

What about using even higher- z lens galaxies? As shown in Fig. 20, for higher- z populations (with $z_L = 2 - 5$) the galaxy-galaxy power spectra are about the same as the shot noise levels. This is true only for the assumed number of lenses, $N_L = 10^6$ (over the full sky), which is somewhat arbitrary. Increasing N_L will help reduce the noise, but only up to a factor of $\sqrt{2}$. For

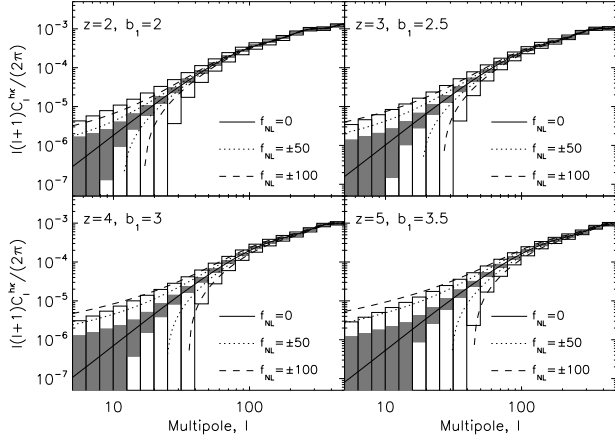


FIG. 21: Same as Fig. 19, but for the high redshift lens galaxies shown in Fig. 16.

populations with $C_l^h \simeq 1/n_L$, we can approximate the variance as

$$\text{Var}(C_l^{h\kappa}) = \frac{(C_l^h + 1/n_L)C_l^\kappa}{(2l+1)\Delta l f_{\text{sky}}} \simeq \frac{2C_l^h C_l^\kappa}{(2l+1)\Delta l f_{\text{sky}}}. \quad (43)$$

Thus, we find $C_l^{h\kappa}/\sqrt{\text{Var}(C_l^{h\kappa})} \gtrsim 1$ when

$$l \gtrsim \frac{1}{r_l \sqrt{(\Delta l/l) f_{\text{sky}}}}. \quad (44)$$

The maximum cross-correlation coefficients are 0.091, 0.084, 0.078, and 0.073 for $z_L = 2, 3, 4$, and 5, respectively. The estimated l_{max} is then 29 ($z_L = 2$), 34 ($z_L = 3$), 38 ($z_L = 4$) and 42 ($z_L = 5$).

In Fig. 21 we compare the expected $1\text{-}\sigma$ uncertainties with the predicted signals from high- z lens galaxies with $f_{\text{NL}} = 0, \pm 50$, and ± 100 . Comparing this result with that in Fig. 19, we conclude that higher- z lens populations do provide a better chance of finding the effects of f_{NL} than lower- z lenses, although we would still need to combine many lens redshift slices. In particular, using higher- z lenses, we can find non-Gaussian effects at higher and higher multipoles which are easier to measure; thus, high- z galaxies correlated with CMB lensing offers a yet another nice probe of the local-type primordial non-Gaussianity.

V. DISCUSSION AND CONCLUSIONS

In this paper we have studied the galaxy-galaxy lensing and galaxy-CMB lensing cross-correlation functions. We have focused on large scales, typically larger than 100 Mpc at the lens redshift. While current measurements have high signal-to-noise ratios on much smaller scales, we believe that future surveys will enable detection of interesting physical effects in the large-scale, linear regime.

We derive the full covariance matrix for galaxy-galaxy lensing, including the cosmic variance due to the clustering of lenses and to cosmic shear (Eq. 18). We use the linear bias model to provide the halo-mass and halo-halo correlations needed for this calculation. We present results for the covariance of the mean tangential shear measurement as a function of angular separations, as well as for the harmonic space halo-convergence cross-power spectrum. Our calculations show that the errors in $\Delta\Sigma(R)$ are dominated by the cosmic variance term for $R \gtrsim 50 h^{-1}$ Mpc (see Fig. 6). Similarly, the errors in the halo-convergence cross power spectra, $C_l^{h\kappa}$, are dominated by the cosmic variance term at $l \lesssim 100$ (see Fig. 19).

For Gaussian initial conditions, we show that the baryonic effects in the matter power spectrum (often called Baryon Acoustic Oscillations) produce a “shoulder” in the galaxy-galaxy lensing correlation (i.e., the mean tangential shears), $\Delta\Sigma(R)$, at $R \sim 110 h^{-1}$ Mpc (see Fig. 3). This effect should be easy to measure from the next-generation lensing surveys by combining $\Delta\Sigma(R)$ from multiple lens redshift slices.

We consider the prospects of detecting primordial non-Gaussianity of the local-form, characterized by the f_{NL} parameter. We have found that the scale-dependent bias from the local-form non-Gaussianity with $f_{\text{NL}} = \pm 50$ modifies $\Delta\Sigma(R)$ at the level of 10–20% at $R \sim 300 h^{-1}$ Mpc (depending on b_1 and z_L ; see Fig. 5) (see Fig. 4). The modification grows rapidly toward larger scales, in proportion to R^2 . High- z galaxies at, e.g., $z \gtrsim 2$, cross-correlated with CMB can be used to find the effects of f_{NL} in the galaxy-convergence power spectrum, $C_l^{h\kappa}$. While the effects are probably too small to see from a single lens redshift (see Fig. 21), many slices can be combined to beat down the cosmic variance errors. Exactly how many slices are necessary, or what is the optimal strategy to measure f_{NL} from the galaxy-CMB lensing signal requires a more detailed study that incorporates the survey strategy for specific galaxy and lens surveys.

We emphasize that, while the two-point statistics of shear fields are not sensitive to primordial non-Gaussianity, the two-point statistics correlating shear fields with density peaks (i.e., galaxies and clusters of galaxies) are sensitive due to the strong scale-dependence of halo bias on large scales.

Finally, we note that one can also measure the effects of f_{NL} on the halo power spectrum, C_l^h . For example, C_l^h that would be measured from LSST can be used to probe $f_{\text{NL}} \sim 1$ [67]; thus, we would expect C_l^h to be more powerful than the lens cross-correlation statistics we studied here. However, a combination of the two measurements would provide useful cross-checks, as galaxy clustering and galaxy-lensing correlations are affected by very different systematics.

Acknowledgments

E.K. would like to thank Erin Sheldon and Rachel Mandelbaum for very useful discussions. B.J. thanks the UT Austin astronomy department and IUCAA for their hospitality while part of this work was carried out, and Gary Bernstein, Sarah Bridle, and Ishaana Monet for stimulating discussions. This material is based in part upon work supported by the Texas Advanced Research Program under Grant No. 003658-0005-2006, by NASA grants NNX08AM29G and NNX08AL43G, and by NSF grants AST-0807649 and PHY-0758153. E.K. acknowledges support from an Alfred P. Sloan Fellowship. D.J. acknowledges support from a Wendell Gordon Endowed Graduate Fellowship of the University of Texas at Austin. B.J. is partially supported by NSF grant AST-0908027.

APPENDIX A: DERIVATION OF THE MEAN TANGENTIAL SHEAR

One may write down the observed tangential shears at a given distance from a lens halo, θ , averaged over N_L lens halos as

$$\gamma_t^h(\theta) = \frac{1}{N_L} \int d^2 \hat{\mathbf{n}} \left[\sum_i^{N_L} \delta_D(\hat{\mathbf{n}} - \hat{\mathbf{n}}_i) \right] \gamma_t(\hat{\mathbf{n}} + \theta), \quad (\text{A1})$$

where δ_D is the delta function, and i denotes the location of lens halos. Note that we have not azimuthally averaged the tangential shears yet. The ensemble average of γ_t^h yields the number-weighted average of the tangential shear:

$$\langle \gamma_t^h \rangle(\theta) = \frac{1}{N_L} \int d^2 \hat{\mathbf{n}} \langle n_L(\hat{\mathbf{n}}) \gamma_t(\hat{\mathbf{n}} + \theta) \rangle, \quad (\text{A2})$$

where $n_L(\hat{\mathbf{n}})$ is the surface number density of lens halos at a given location on the sky, $\hat{\mathbf{n}}$. Expanding it into the perturbation, $n_L(\hat{\mathbf{n}}) = \bar{n}_L[1 + \delta_h(\hat{\mathbf{n}})]$, we obtain

$$\langle \gamma_t^h \rangle(\theta) = \frac{1}{f_{\text{sky}}} \int \frac{d^2 \hat{\mathbf{n}}}{4\pi} \langle \delta_h(\hat{\mathbf{n}}) \gamma_t(\hat{\mathbf{n}} + \theta) \rangle, \quad (\text{A3})$$

where $f_{\text{sky}} \equiv N_L/(4\pi\bar{n}_L)$ is a fraction of sky covered by the observation. From statistical isotropy of the universe, $\langle \delta_h(\hat{\mathbf{n}}) \gamma_t(\hat{\mathbf{n}} + \theta) \rangle$ does not depend on $\hat{\mathbf{n}}$, and thus the integral over $\hat{\mathbf{n}}$ simply gives $4\pi f_{\text{sky}}$. Expanding δ_h and γ_t in Fourier space, we obtain

$$\begin{aligned} & \langle \gamma_t^h \rangle(\theta) \\ &= - \int \frac{d^2 \mathbf{l}}{(2\pi)^2} \frac{d^2 \mathbf{l}'}{(2\pi)^2} e^{i\mathbf{l} \cdot \hat{\mathbf{n}}} e^{i\mathbf{l}' \cdot (\hat{\mathbf{n}} + \theta)} \cos[2(\phi - \varphi)] \langle \delta_h(\mathbf{l}) \kappa(\mathbf{l}') \rangle \\ &= - \int \frac{d^2 \mathbf{l}}{(2\pi)^2} C_l^{h\kappa} \cos[2(\phi - \varphi)] e^{-i\mathbf{l} \cdot \theta}, \end{aligned} \quad (\text{A4})$$

where we have used $\langle \delta_h(\mathbf{l}) \kappa(\mathbf{l}') \rangle = (2\pi)^2 C_l^{h\kappa} \delta_D(\mathbf{l} + \mathbf{l}')$. Finally, we take the azimuthal average of $\langle \gamma_t^h \rangle(\theta)$ to find

the averaged mean tangential shear:

$$\begin{aligned} \langle \overline{\gamma}_t^h \rangle(\theta) &= \int_0^{2\pi} \frac{d\phi}{2\pi} \langle \gamma_t^h \rangle(\theta) \\ &= - \int \frac{d^2 \mathbf{l}}{(2\pi)^2} C_l^{h\kappa} \int_0^{2\pi} \frac{d\phi}{2\pi} \cos[2(\phi - \varphi)] e^{-i\mathbf{l} \cdot \theta \cos(\phi - \varphi)} \\ &= \int \frac{d^2 \mathbf{l}}{(2\pi)^2} C_l^{h\kappa} J_2(l\theta) \\ &= \int \frac{l dl}{2\pi} C_l^{h\kappa} J_2(l\theta). \end{aligned} \quad (\text{A5})$$

This completes the derivation of Eq. (11).

APPENDIX B: DERIVATION OF THE COVARIANCE MATRIX OF THE MEAN TANGENTIAL SHEAR

To compute the covariance matrix of the tangential shears (not yet azimuthally averaged), we first compute

$$\begin{aligned} & \langle \gamma_t^h(\theta) \gamma_t^h(\theta') \rangle \\ &= \frac{1}{N_L^2} \sum_{ij} \int d^2 \hat{\mathbf{n}} \int d^2 \hat{\mathbf{n}}' \\ & \quad \times \langle \delta_D(\hat{\mathbf{n}} - \hat{\mathbf{n}}_i) \delta_D(\hat{\mathbf{n}}' - \hat{\mathbf{n}}_j) \gamma_t(\hat{\mathbf{n}} + \theta) \gamma_t(\hat{\mathbf{n}}' + \theta') \rangle \\ &= \frac{1}{N_L^2} \int d^2 \hat{\mathbf{n}} \int d^2 \hat{\mathbf{n}}' \\ & \quad \times [\delta_D(\hat{\mathbf{n}} - \hat{\mathbf{n}}') \langle n_L(\hat{\mathbf{n}}) \gamma_t(\hat{\mathbf{n}} + \theta) \gamma_t(\hat{\mathbf{n}}' + \theta') \rangle \\ & \quad + \langle n_L(\hat{\mathbf{n}}) n_L(\hat{\mathbf{n}}') \gamma_t(\hat{\mathbf{n}} + \theta) \gamma_t(\hat{\mathbf{n}}' + \theta') \rangle]. \end{aligned} \quad (\text{B1})$$

Here, the first term in the square bracket correlates two γ_t 's measured relative to the same lens halo (1-halo term), and the second correlates two γ_t 's relative to two lens halos (2-halo term). Again expanding n_L into the perturbation, $n_L(\hat{\mathbf{n}}) = \bar{n}_L[1 + \delta_h(\hat{\mathbf{n}})]$, we obtain

$$\begin{aligned} & \langle \gamma_t(\theta) \gamma_t(\theta') \rangle \\ &= \frac{1}{f_{\text{sky}}} \frac{1}{N_L} \int \frac{d^2 \hat{\mathbf{n}}}{4\pi} \langle \gamma_t(\hat{\mathbf{n}} + \theta) \gamma_t(\hat{\mathbf{n}} + \theta') \rangle \\ & \quad + \frac{1}{f_{\text{sky}}^2} \int \frac{d^2 \hat{\mathbf{n}}}{4\pi} \int \frac{d^2 \hat{\mathbf{n}}'}{4\pi} [\langle \gamma_t(\hat{\mathbf{n}} + \theta) \gamma_t(\hat{\mathbf{n}}' + \theta') \rangle \\ & \quad + \langle \delta_h(\hat{\mathbf{n}}) \delta_h(\hat{\mathbf{n}}') \gamma_t(\hat{\mathbf{n}} + \theta) \gamma_t(\hat{\mathbf{n}}' + \theta') \rangle]. \end{aligned} \quad (\text{B2})$$

Here, we assume that δ_h and γ_t obey Gaussian statistics, i.e., $\langle \delta_h \gamma_t \gamma_t \rangle = 0$. This approximation is justified even in the presence of primordial non-Gaussianity, as non-Gaussianity is weak, and this approximation only affects the size of errorbars. Let us evaluate each term. With γ_t expanded in Fourier space, the first term (1-halo term)

becomes

$$\begin{aligned} & \frac{1}{N_L} \frac{1}{f_{\text{sky}}} \int \frac{d^2 \hat{\mathbf{n}}}{4\pi} \langle \gamma_t(\hat{\mathbf{n}} + \boldsymbol{\theta}) \gamma_t(\hat{\mathbf{n}} + \boldsymbol{\theta}') \rangle \\ &= \frac{1}{N_L} \int \frac{d^2 \mathbf{l}}{(2\pi)^2} C_l^\kappa \cos[2(\phi - \varphi)] \cos[2(\phi' - \varphi)] e^{i\mathbf{l} \cdot (\boldsymbol{\theta} - \boldsymbol{\theta}')} \\ & \quad + \frac{\sigma_\gamma^2}{N_L n_S} \delta_D(\boldsymbol{\theta} - \boldsymbol{\theta}'), \end{aligned} \quad (\text{B3})$$

where σ_γ is the r.m.s. shape noise (dimensionless), and n_S is the surface density of source (background) galaxies that are available for the shear measurement at a given location. By azimuthally averaging γ_t , we find

$$\begin{aligned} & \frac{1}{N_L} \int_0^{2\pi} \frac{d\phi}{2\pi} \int_0^{2\pi} \frac{d\phi'}{2\pi} \langle \gamma_t(\hat{\mathbf{n}} + \boldsymbol{\theta}) \gamma_t(\hat{\mathbf{n}} + \boldsymbol{\theta}') \rangle \\ &= \frac{1}{N_L} \int \frac{d^2 \mathbf{l}}{(2\pi)^2} C_l^\kappa J_2(l\theta) J_2(l\theta') \\ & \quad + \frac{\sigma_\gamma^2}{N_L n_S} \frac{\delta_D(\theta - \theta')}{2\pi\theta}. \end{aligned} \quad (\text{B4})$$

Here, C_l^κ is the angular power spectrum of $\kappa(\mathbf{l})$.

As for the second term (2-halo term), the first of the second term vanishes, as $\int d^2 \hat{\mathbf{n}} \gamma_t(\hat{\mathbf{n}} + \boldsymbol{\theta}) = 0$. The remaining non-vanishing term gives

$$\begin{aligned} & \frac{1}{f_{\text{sky}}^2} \int \frac{d^2 \hat{\mathbf{n}}}{4\pi} \int \frac{d^2 \hat{\mathbf{n}}'}{4\pi} \\ & \times [\langle \delta_h(\hat{\mathbf{n}}) \gamma_t(\hat{\mathbf{n}} + \boldsymbol{\theta}) \rangle \langle \delta_h(\hat{\mathbf{n}}') \gamma_t(\hat{\mathbf{n}}' + \boldsymbol{\theta}') \rangle \\ & \quad + \langle \delta_h(\hat{\mathbf{n}}) \gamma_t(\hat{\mathbf{n}}' + \boldsymbol{\theta}') \rangle \langle \delta_h(\hat{\mathbf{n}}') \gamma_t(\hat{\mathbf{n}} + \boldsymbol{\theta}) \rangle \\ & \quad + \langle \delta_h(\hat{\mathbf{n}}) \delta_h(\hat{\mathbf{n}}') \rangle \langle \gamma_t(\hat{\mathbf{n}} + \boldsymbol{\theta}) \gamma_t(\hat{\mathbf{n}}' + \boldsymbol{\theta}') \rangle] \\ &= \langle \gamma_t^h(\boldsymbol{\theta}) \rangle \langle \gamma_t^h(\boldsymbol{\theta}') \rangle \\ & \quad + \frac{1}{4\pi f_{\text{sky}}} \int \frac{d^2 \mathbf{l}}{(2\pi)^2} \cos[2(\phi - \varphi)] \cos[2(\phi' - \varphi)] e^{i\mathbf{l} \cdot (\boldsymbol{\theta} - \boldsymbol{\theta}')} \\ & \quad \times \left[(C_l^{h\kappa})^2 + C_l^h \left(C_l^\kappa + \frac{\sigma_\gamma^2}{n_S} \right) \right]. \end{aligned} \quad (\text{B5})$$

Here, C_l^h is the angular power spectrum of $\delta_h(\mathbf{l})$. By azimuthally averaging γ_t in the above equation, we find

$$\begin{aligned} & \langle \bar{\gamma}_t^h(\boldsymbol{\theta}) \rangle \langle \bar{\gamma}_t^h(\boldsymbol{\theta}') \rangle \\ & + \frac{1}{4\pi f_{\text{sky}}} \int \frac{d^2 \mathbf{l}}{(2\pi)^2} J_2(l\theta) J_2(l\theta') \\ & \quad \times \left[(C_l^{h\kappa})^2 + C_l^h \left(C_l^\kappa + \frac{\sigma_\gamma^2}{n_S} \right) \right], \end{aligned} \quad (\text{B6})$$

where we have used the identity

$$\frac{\delta_D(\theta - \theta')}{2\pi\theta} = \int \frac{ldl}{2\pi} J_2(l\theta) J_2(l\theta'). \quad (\text{B7})$$

Collecting both the 1-halo and 2-halo terms, we finally obtain the covariance matrix of the azimuthally-averaged

mean tangential shear:

$$\begin{aligned} & \langle \bar{\gamma}_t^h(\boldsymbol{\theta}) \bar{\gamma}_t^h(\boldsymbol{\theta}') \rangle - \langle \bar{\gamma}_t^h(\boldsymbol{\theta}) \rangle \langle \bar{\gamma}_t^h(\boldsymbol{\theta}') \rangle \\ &= \frac{1}{4\pi f_{\text{sky}}} \int \frac{ldl}{2\pi} J_2(l\theta) J_2(l\theta') \\ & \quad \times \left[(C_l^{h\kappa})^2 + \left(C_l^h + \frac{1}{n_L} \right) \left(C_l^\kappa + \frac{\sigma_\gamma^2}{n_S} \right) \right]. \end{aligned}$$

This completes the derivation of Eq. (18).

APPENDIX C: ON THE ACCURACY OF LIMBER'S APPROXIMATION

Throughout this paper we have repeatedly used Limber's approximation in order to relate the angular correlation function to the corresponding three dimensional power spectrum. In general, Limber's approximation is known to be accurate only for small angular scales, and only for the quantities which are integrated over a broad range of redshift.

However, the situations we have considered in this paper sometimes violate both of the conditions above: 1) We correlate the convergence field with galaxies within a very thin redshift slice, and 2) the non-Gaussianity signal we study in this paper appears only on very large scales.

Then, how accurate is Limber's approximation in this case? In this Appendix, we shall study in detail the validity and limitation of Limber's approximation, by comparing the main results of the paper to the result of *exact* calculations.

Consider a quantity $x_i(\hat{\mathbf{n}})$, which is projected on the sky. Here, $\hat{\mathbf{n}}$ is the unit vector pointing toward a given direction on the sky. This quantity is related to the three dimensional quantity $s_i(\mathbf{r}; z)$ by a projection kernel $W_i(z)$ as

$$x_i(\hat{\mathbf{n}}) = \int dz W_i(z) s_i[d_A(z) \hat{\mathbf{n}}; z]. \quad (\text{C1})$$

Throughout this Appendix, we use $d_A(z)$ to denote $d_A(0; z)$.

Fourier transforming $s_i(\mathbf{r})$, one obtains

$$\begin{aligned} & s_i[d_A(z) \hat{\mathbf{n}}; z] \\ &= \int \frac{d^3 \mathbf{k}}{(2\pi)^3} s_i(\mathbf{k}, z) e^{i\mathbf{k} \cdot \hat{\mathbf{n}} d_A(z)} \\ &= 4\pi \sum_{l,m} i^l \int \frac{d^3 k}{(2\pi)^3} s_i(\mathbf{k}, z) j_l[k d_A(z)] Y_{lm}^*(\hat{\mathbf{k}}) Y_{lm}(\hat{\mathbf{n}}) \end{aligned}$$

In the third line, we have used Rayleigh's formula:

$$e^{i\mathbf{k} \cdot \hat{\mathbf{n}} r} = 4\pi \sum_{l,m} i^l j_l(kr) Y_{lm}^*(\hat{\mathbf{k}}) Y_{lm}(\hat{\mathbf{n}}).$$

By using Eq. (C2), we rewrite Eq. (C1) as

$$x_i(\hat{\mathbf{n}}) = 4\pi \sum_{l,m} i^l \int dz W_i(z) \times \int \frac{d^3 k}{(2\pi)^3} s_i(\mathbf{k}, z) j_l[kd_A(z)] Y_{lm}^*(\hat{\mathbf{k}}) Y_{lm}(\hat{\mathbf{n}}) \quad (\text{C3})$$

Therefore, the coefficients of the spherical harmonics decomposition of $x_i(\hat{\mathbf{n}})$, $a_{lm}^{x_i}$, becomes

$$a_{lm}^{x_i} = 4\pi i^l \int dz W_i(z) \int \frac{d^3 k}{(2\pi)^3} s_i(\mathbf{k}, z) j_l[kd_A(z)] Y_{lm}^*(\hat{\mathbf{k}}). \quad (\text{C4})$$

We calculate the angular power spectrum, $C_l^{x_i x_j}$, by taking an ensemble average of $\langle a_{lm}^{x_i} a_{lm}^{x_j*} \rangle$ as

$$\begin{aligned} C_l^{x_i x_j} &\equiv \langle a_{lm}^{x_i} a_{lm}^{x_j*} \rangle \\ &= (4\pi)^2 \int dz W_i(z) \int dz' W_j(z') \int \frac{d^3 k}{(2\pi)^3} P^{s_i s_j}(\mathbf{k}; z, z') \\ &\quad \times j_l[kd_A(z)] j_l[kd_A(z')] Y_{lm}^*(\hat{\mathbf{k}}) Y_{lm}(\hat{\mathbf{k}}), \end{aligned} \quad (\text{C5})$$

where we have used the definition of the power spectrum:

$$\langle s_i(\mathbf{k}, z) s_j^*(\mathbf{k}', z) \rangle \equiv (2\pi)^3 \delta(\mathbf{k} - \mathbf{k}') P^{s_i s_j}(\mathbf{k}; z, z').$$

Now, by assuming statistical isotropy of the universe, we write $P^{s_i s_j}(\mathbf{k}; z, z') = P^{s_i s_j}(k; z, z')$, and do the angular integration of $\hat{\mathbf{k}}$ by using the orthonormality condition of spherical harmonics:

$$\int d\hat{\mathbf{k}} Y_{lm}(\hat{\mathbf{k}}) Y_{lm}^*(\hat{\mathbf{k}}) = 1.$$

We then obtain the angular power spectrum given by

$$\begin{aligned} C_l^{x_i x_j} &= \int dz W_i(z) \int dz' W_j(z') \\ &\quad \times \left\{ \frac{2}{\pi} \int k^2 dk P^{s_i s_j}(k; z, z') j_l[kd_A(z)] j_l[kd_A(z')] \right\}. \end{aligned}$$

This is the *exact* relation.

What determines the form of $W_i(z)$? For a projected galaxy distribution projected on the sky, this kernel is simply a normalized galaxy distribution function in redshift space. In this paper, we consider the delta function-like distribution, i.e.,

$$W_g(z) = \delta^D(z - z_L). \quad (\text{C7})$$

Using Eq. (C6) with the delta function kernel above yields Eq. (36):

$$C_l^h = \frac{2}{\pi} \int dk k^2 P_g(k, z_L) j_l^2[kd_A(z_L)]. \quad (\text{C8})$$

Again, this is still the exact result. As the form of $W_g(z)$ we have considered here (i.e., a delta function)

is a sharply peaked function, we cannot use Limber's approximation given below. This is the reason why we have used the exact result for C_l^h .

In order to get the expression for Limber's approximation, we assume that $P^{s_i s_j}(k)$ is a slowly-varying function of k . Then, by using the identity

$$\frac{2}{\pi} \int k^2 dk j_l(kr) j_l(kr') = \frac{\delta^D(r - r')}{r^2}, \quad (\text{C9})$$

we approximate the k integral of Eq. (C6) as

$$\begin{aligned} &\frac{2}{\pi} \int k^2 dk P^{s_i s_j}(k) j_l(kr) j_l(kr') \\ &\approx \frac{\delta^D(r - r')}{r^2} P^{s_i s_j} \left(k = \frac{l + 1/2}{r} \right). \end{aligned} \quad (\text{C10})$$

By using this approximation, we finally get

$$C_l^{x_i x_j} \approx \int dz W_i(z) W_j(z) \frac{H(z)}{d_A^2(z)} P^{s_i s_j} \left(k = \frac{l + 1/2}{r}; z \right), \quad (\text{C11})$$

which is the result known as Limber's approximation.

One important application of Limber's approximation is the statistics involving weak gravitational lensing. The lensing kernel for the convergence field, $W_\kappa(z)$, can be calculated by integrating the lens equation:

$$W_\kappa(z) = \frac{\rho_0}{\Sigma_c(z; z_S) H(z)}, \quad (\text{C12})$$

where $\Sigma_c(z; z_S)$ is the critical surface density defined in Eq. (16). The exact result for the galaxy-convergence angular cross power spectrum is

$$\begin{aligned} C_l^{h\kappa}(z_L) &= \frac{2}{\pi} \int_0^{z_S} dz \frac{\rho_0}{\Sigma_c(z; z_S) H(z)} \\ &\quad \times \int dk k^2 P_{hm}(k, z_L, z) j_l[kd_A(z_L)] j_l[kd_A(z)], \end{aligned} \quad (\text{C13})$$

(C6) and the exact result for the convergence-convergence angular power spectrum is

$$\begin{aligned} C_l^\kappa(z_S) &= \frac{2}{\pi} \int_0^{z_S} dz \int_0^{z_S} dz' \frac{\rho_0^2}{\Sigma_c(z; z_S) H(z) \Sigma_c(z'; z_S) H(z')} \\ &\quad \times \int dk k^2 P_m(k, z, z') j_l[kd_A(z)] j_l[kd_A(z')]. \end{aligned} \quad (\text{C14})$$

First, we compare the exact convergence-convergence angular power spectrum to Limber's approximation. Fig. 22 shows that Limber's approximation works very well for all four source redshifts we study in the paper: $z_S = 0.65, 1.19, 2.25$, and 1089.0 . For $l > 10$, the error caused by Limber's approximation is always much smaller than 1%.

Then, we compare the galaxy-convergence cross angular power spectra. Fig. 23 and Fig. 24 show the comparison between the exact galaxy-convergence cross power

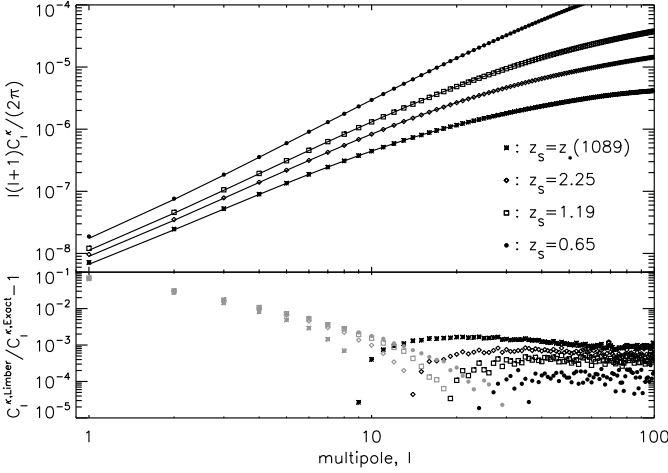


FIG. 22: Top: Convergence-convergence angular power spectrum from two different methods: the exact calculation (Eq. C14, symbols) and Limber's approximation (Eq. 35, solid lines). Bottom: Fractional differences between Limber's approximation and the exact integration. Symbols are the same as the top panel. Grey symbols show the absolute values of negative values.

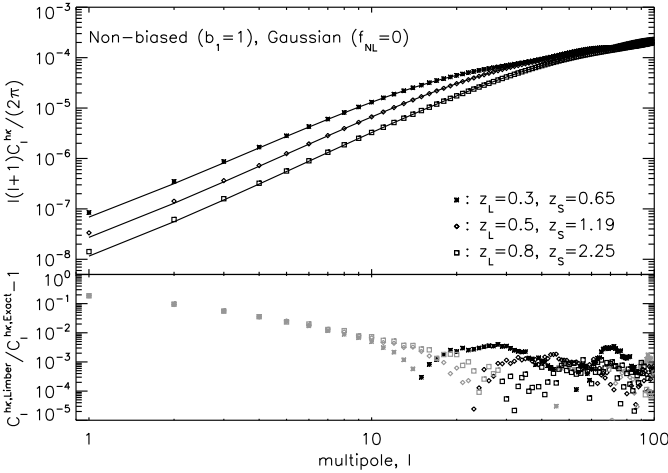


FIG. 23: Same as Fig. 22, but for the galaxy-convergence cross angular power spectrum with $f_{NL} = 0$ and $b_1 = 1$.

spectrum (Eq. C13, symbols) and their Limber approximation (Eq. 32, solid lines) for three galaxy-galaxy lensing cases we study in Sec. II: $(z_L, z_S) = (0.3, 0.65)$, $(0.5, 1.19)$, and $(0.8, 2.25)$.

For the Gaussian term (Fig. 23), Limber's approximation is accurate at $l > 10$ with the errors less than 1%. On the other hand, Limber's approximation to the non-Gaussian correction term (Fig. 24) has a sizable error, at the level of 10%, at $l \sim 10$. The error goes down to the 1% level only at $l \sim 100$. One needs to keep this in mind when comparing Limber's approximation with observa-

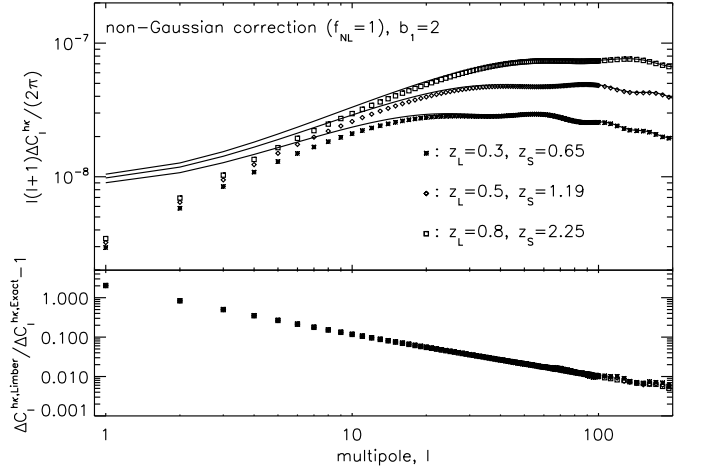


FIG. 24: Same as Fig. 22, but for the non-Gaussian correction (i.e., the term proportional to $\Delta b(k)$) to the galaxy-convergence cross angular power spectrum. We show the corrections with $f_{NL} = 1$ and $b_1 = 2$.

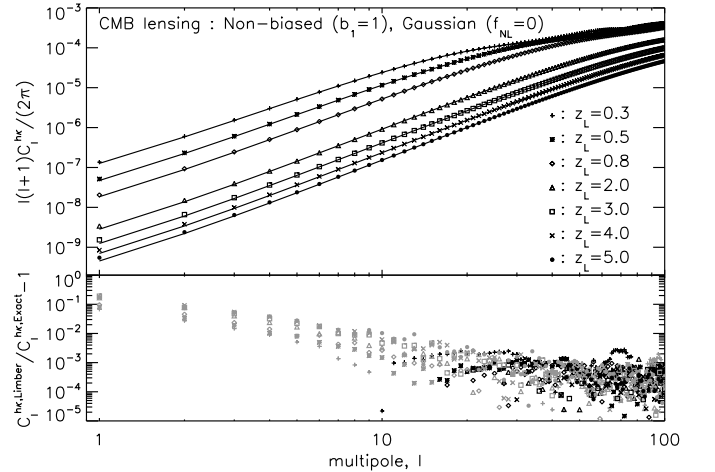


FIG. 25: Same as Fig. 23, but for the galaxy-CMB lensing.

tions. We find that Limber's approximation underpredicts the Gaussian term at $l \lesssim 20$, while it overpredicts the non-Gaussian corrections at all multipoles.

The story is basically the same for the galaxy-CMB lensing cross power spectrum. Fig. 25 (Gaussian term) and Fig. 26 (non-Gaussian correction) show the comparison between the exact galaxy-convergence cross power spectrum (Eq. C13, solid lines) and their Limber approximation (Eq. 32, dashed lines) for seven lens redshifts we study in Sec. IV: $z_L = 0.3, 0.5, 0.8, 2, 3, 4$, and 5 . Again, for small scales, $l > 10$, Limber's approximation works better than 1% for the Gaussian term, while it overpredicts the non-Gaussian correction at the level of 10% at $l \sim 10$ and 1% at $l \sim 100$.

What about the effect on the mean tangential shear,

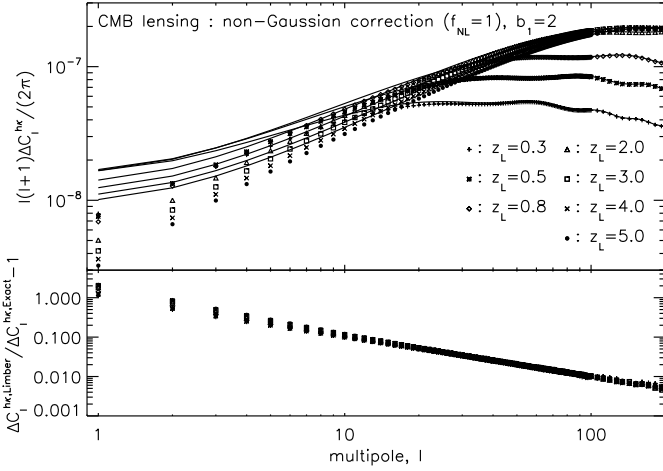


FIG. 26: Same as Fig. 24, but for the galaxy-CMB lensing.

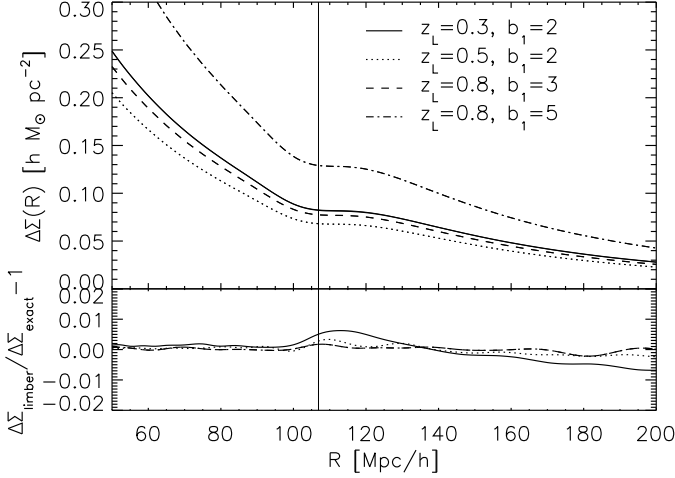


FIG. 27: Top: Same as Fig. 3, but also showing the exact result (Eq. C13, thick lines) on top of the result from Limber's approximation (Eq. 32, thin lines). Bottom: Fractional difference of Limber's approximation relative to the exact result.

$\Delta\Sigma(R)$? Fig. 27 compares the Gaussian term of $\Delta\Sigma(R)$ from the exact integration and that from Limber's approximation. On the top panel of Fig. 27, we show the baryonic feature computed with Limber's approximation (thin lines, the same as those in Fig. 3) as well as that computed with the exact integration (thick lines). They are indistinguishable by eyes. The bottom panel shows the fractional differences between the two. We find that Limber's approximation is better than 0.5% for $R < 180 h^{-1} \text{ Mpc}$; thus, the baryonic feature in $\Delta\Sigma$ is not an artifact caused by Limber's approximation.

However, Limber's approximation becomes worse and worse as we go to larger R . Fig. 29 shows $\Delta\Sigma$ on large scales. For the lens redshifts that we have studied here,

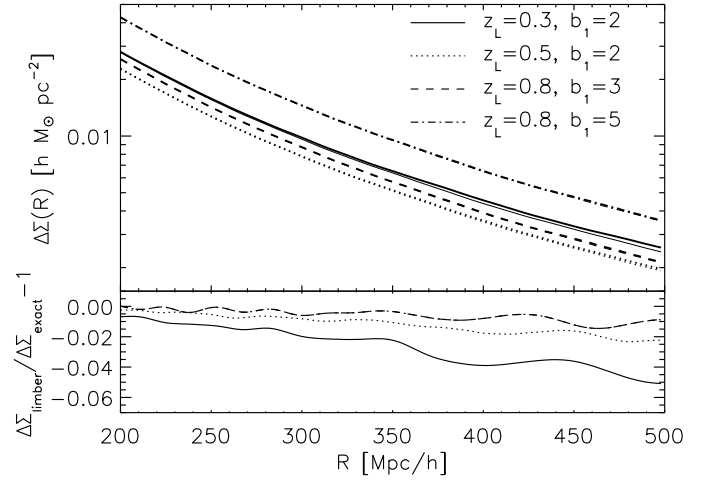


FIG. 28: Same as Fig. 27, but for larger R . Thick lines are the results of the exact integration, while the thin lines are Limber's approximation. The Limber approximation overpredicts $\Delta\Sigma(R)$ for large R , but the error is at most 5% for $R < 500 h^{-1} \text{ Mpc}$. The error is the largest for the lowest z_L , as a physical separation R at a lower redshift corresponds to a larger angular separation on the sky.

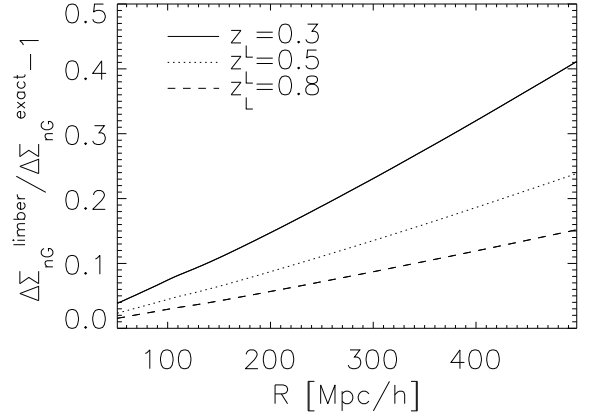


FIG. 29: Fractional differences in the non-Gaussian correction terms, $\Delta\Sigma_{\text{NG}}$, from Limber's approximation and the exact integration. Using Limber's approximation, we overpredict the non-Gaussian correction by $\sim 20\%$ at $R = 300 h^{-1} \text{ Mpc}$ for $z_L = 0.3$.

the error is at most 5% for $R < 500 h^{-1} \text{ Mpc}$, and the error is the largest for the lowest z_L , as a given R at a lower redshift corresponds to a larger angular separation on the sky.

While Limber's approximation underpredicts the Gaussian term on large scales, it overpredicts the non-Gaussian correction terms. Fig. 29 shows the fractional differences of the non-Gaussian correction terms, $\Delta\Sigma_{\text{NG}}$,

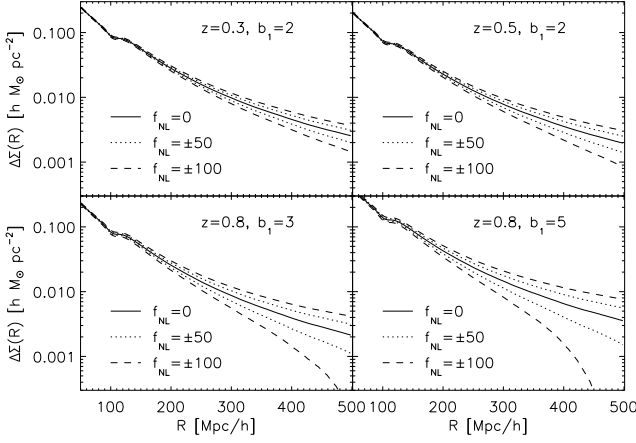


FIG. 30: Same as Fig. 4, but with the exact integration instead of Limber's approximation.

between Limber's approximation and the exact calculation as a function of separation R for three lens redshifts: $z_L = 0.3, 0.5$, and 0.8 . This figure shows that the error caused by Limber's approximation can be substantial on $\Delta\Sigma_{\text{nG}}$.

As Limber's approximation to $\Delta\Sigma(R)$ can be quite inaccurate on very large scales, we show the exact calculations of $\Delta\Sigma(R)$ in Fig. 30. (Limber's approximation is given in Fig. 4.)

Finally, we note that the definition of the tangential shear we have used (Eq. 4) is valid only on the flat sky (as noted in the footnote there), and thus the prediction for $\Delta\Sigma$ on very large scales probably needs to be revisited with the exact definition of the tangential shears on the full sky using the spin-2 harmonics. This is beyond of the scope of our paper.

-
- [1] E. Komatsu and D. N. Spergel, Phys. Rev. D **63**, 63002 (2001)
 - [2] E. Komatsu, J. Dunkley, M. R.olta, C. L. Bennett, B. Gold, G. Hinshaw, N. Jarosik, D. Larson, M. Limon, L. Page, et al., Astrophys. J. Suppl. **180**, 330 (2009), 0803.0547.
 - [3] D. Babich, P. Creminelli, and M. Zaldarriaga, JCAP **0408**, 009 (2004), astro-ph/0405356.
 - [4] D. S. Salopek and J. R. Bond, Phys. Rev. D **42**, 3936 (1990)
 - [5] T. Falk, R. Rangarajan, and M. Srednicki, Astrophys. J. Lett. **403**, L1 (1993)
 - [6] A. Gangui, F. Lucchin, S. Matarrese, and S. Mollerach, Astrophys. J. **430**, 447 (1994)
 - [7] J. M. Maldacena, JHEP **05**, 013 (2003), astro-ph/0210603.
 - [8] V. Acquaviva, N. Bartolo, S. Matarrese, and A. Riotto, Nucl. Phys. **B667**, 119 (2003), astro-ph/0209156.
 - [9] P. Creminelli and M. Zaldarriaga (2004), astro-ph/0405428.
 - [10] D. Seery and J. E. Lidsey, JCAP **0506**, 003 (2005), astro-ph/0503692.
 - [11] X. Chen, M.-x. Huang, S. Kachru, and G. Shiu, JCAP **0701**, 002 (2007), hep-th/0605045.
 - [12] C. Cheung, P. Creminelli, A. L. Fitzpatrick, J. Kaplan, and L. Senatore, JHEP **03**, 014 (2008), 0709.0293.
 - [13] N. Bartolo, E. Komatsu, S. Matarrese, and A. Riotto, Phys. Rept. **402**, 103 (2004), astro-ph/0406398.
 - [14] E. Komatsu et al. (2009), 0902.4759.
 - [15] K. M. Smith, L. Senatore, and M. Zaldarriaga, ArXiv e-prints (2009), 0901.2572.
 - [16] L. Verde, L. Wang, A. F. Heavens, and M. Kamionkowski, Mon. Not. R. Astron. Soc. **313**, 141 (2000), arXiv:astro-ph/9906301.
 - [17] L. Wang and M. Kamionkowski, Phys. Rev. D **61**, 63504 (2000)
 - [18] E. Komatsu, B. D. Wandelt, D. N. Spergel, A. J. Banday, and K. M. Górski, Astrophys. J. **566**, 19 (2002)
 - [19] E. Komatsu, A. Kogut, M. R. Nolta, C. L. Bennett, M. Halpern, G. Hinshaw, N. Jarosik, M. Limon, S. S. Meyer, L. Page, et al., Astrophys. J. Suppl. **148**, 119 (2003).
 - [20] E. Komatsu, ArXiv Astrophysics e-prints (2001), ph.D. thesis at Tohoku University (astro-ph/0206039)
 - [21] T. Okamoto and W. Hu, Phys. Rev. D **66**, 063008 (2002), arXiv:astro-ph/0206155.
 - [22] N. Kogo and E. Komatsu, Phys. Rev. **D73**, 083007 (2006), astro-ph/0602099.
 - [23] R. Scoccimarro, E. Sefusatti, and M. Zaldarriaga, Phys. Rev. D **69**, 103513 (2004).
 - [24] E. Sefusatti and E. Komatsu, Phys. Rev. D **76**, 083004 (2007), arXiv:0705.0343.
 - [25] D. Jeong and E. Komatsu, Astrophys. J. **703**, 1230 (2009), 0904.0497.
 - [26] E. Sefusatti, ArXiv e-prints (2009), 0905.0717.
 - [27] F. Lucchin and S. Matarrese, Astrophys. J. **330**, 535 (1988)
 - [28] S. Matarrese, L. Verde, and R. Jimenez, Astrophys. J. **541**, 10 (2000)
 - [29] E. Sefusatti, C. Vale, K. Kadota, and J. Frieman, Astrophys. J. **658**, 669 (2007), astro-ph/0609124.
 - [30] M. LoVerde, A. Miller, S. Shandera, and L. Verde, JCAP **0804**, 014 (2008), 0711.4126.
 - [31] N. Dalal, O. Doré, D. Huterer, and A. Shirokov, Phys. Rev. D **77**, 123514 (2008), 0710.4560.
 - [32] S. Matarrese and L. Verde, Astrophys. J. Lett. **677**, L77 (2008), 0801.4826.
 - [33] A. Slosar, C. Hirata, U. Seljak, S. Ho, and N. Padmanabhan, Journal of Cosmology and Astro-Particle Physics **8**, 31 (2008), 0805.3580.
 - [34] N. Afshordi and A. J. Tolley, Phys. Rev. D **78**, 123507 (2008), 0806.1046.
 - [35] A. Taruya, K. Koyama, and T. Matsubara, Phys. Rev. **D78**, 123534 (2008), 0808.4085.
 - [36] V. Desjacques, U. Seljak, and I. T. Iliev, ArXiv e-prints (2008), 0811.2748.
 - [37] A. Pillepich, C. Porciani, and O. Hahn, ArXiv e-prints (2008), 0811.4176.
 - [38] M. Grossi, L. Verde, C. Carbone, K. Dolag, E. Branchini, F. Iannuzzi, S. Matarrese, and L. Moscardini, ArXiv e-

- prints (2009), 0902.2013.
- [39] M. Bartelmann and P. Schneider, *Phys. Rep.* **340**, 291 (2001).
 - [40] J. A. Tyson, F. Valdes, J. F. Jarvis, and A. P. Mills, Jr., *Astrophys. J. Lett.* **281**, L59 (1984).
 - [41] T. G. Brainerd, R. D. Blandford, and I. Smail, *Astrophys. J.* **466**, 623 (1996), arXiv:astro-ph/9503073.
 - [42] T. A. McKay, E. S. Sheldon, J. Racusin, P. Fischer, U. Seljak, A. Stebbins, D. Johnston, J. A. Frieman, N. Bahcall, J. Brinkmann, et al., *ArXiv Astrophysics e-prints* (2001), arXiv:astro-ph/0108013.
 - [43] J. Guzik and U. Seljak, *Mon. Not. R. Astron. Soc.* **335**, 311 (2002), arXiv:astro-ph/0201448.
 - [44] E. S. Sheldon, D. E. Johnston, J. A. Frieman, R. Scranton, T. A. McKay, A. J. Connolly, T. Budavári, I. Zehavi, N. A. Bahcall, J. Brinkmann, et al., *Astron. J.* **127**, 2544 (2004), arXiv:astro-ph/0312036.
 - [45] R. Mandelbaum, U. Seljak, G. Kauffmann, C. M. Hirata, and J. Brinkmann, *Mon. Not. R. Astron. Soc.* **368**, 715 (2006), arXiv:astro-ph/0511164.
 - [46] R. Mandelbaum, U. Seljak, R. J. Cool, M. Blanton, C. M. Hirata, and J. Brinkmann, *Mon. Not. R. Astron. Soc.* **372**, 758 (2006), arXiv:astro-ph/0605476.
 - [47] A. Stebbins, *ArXiv Astrophysics e-prints* (1996), arXiv:astro-ph/9609149.
 - [48] E. S. Sheldon, D. E. Johnston, R. Scranton, B. P. Koester, T. A. McKay, H. Oyaizu, C. Cunha, M. Lima, H. Lin, J. A. Frieman, et al., *ArXiv e-prints* (2007), 0709.1153.
 - [49] D. E. Johnston, E. S. Sheldon, R. H. Wechsler, E. Rozo, B. P. Koester, J. A. Frieman, T. A. McKay, A. E. Evrard, M. R. Becker, and J. Annis, *ArXiv e-prints* (2007), 0709.1159.
 - [50] W. Hu and B. Jain, *Phys. Rev. D* **70**, 043009 (2004), arXiv:astro-ph/0312395.
 - [51] D. N. Limber, *Astrophys. J.* **119**, 655 (1954).
 - [52] N. Kaiser, *Astrophys. J.* **388**, 272 (1992).
 - [53] M. Tegmark, D. J. Eisenstein, M. A. Strauss, D. H. Weinberg, M. R. Blanton, J. A. Frieman, M. Fukugita, J. E. Gunn, A. J. S. Hamilton, G. R. Knapp, et al., *Phys. Rev. D* **74**, 123507 (2006), arXiv:astro-ph/0608632.
 - [54] D. Schlegel, M. White, and D. Eisenstein, *ArXiv e-prints* (2009), 0902.4680.
 - [55] H. Zhan, *Journal of Cosmology and Astro-Particle Physics* **8**, 8 (2006), arXiv:astro-ph/0605696.
 - [56] D. J. Eisenstein and W. Hu, *Astrophys. J.* **496**, 605 (1998).
 - [57] A. Lewis and A. Challinor, *Phys. Rep.* **429**, 1 (2006), arXiv:astro-ph/0601594.
 - [58] W. Hu and T. Okamoto, *Astrophys. J.* **574**, 566 (2002), arXiv:astro-ph/0111606.
 - [59] T. Okamoto and W. Hu, *Phys. Rev. D* **67**, 83002 (2003).
 - [60] C. M. Hirata and U. Seljak, *Phys. Rev. D* **68**, 083002 (2003), astro-ph/0306354.
 - [61] S. Boughn and R. Crittenden, *Nature (London)* **427**, 45 (2004).
 - [62] R. Mandelbaum, C. M. Hirata, U. Seljak, J. Guzik, N. Padmanabhan, C. Blake, M. R. Blanton, R. Lupton, and J. Brinkmann, *Mon. Not. R. Astron. Soc.* **361**, 1287 (2005), arXiv:astro-ph/0501201.
 - [63] G. J. Hill, K. Gebhardt, E. Komatsu, and P. J. MacQueen, **743**, 224 (2004).
 - [64] G. J. Hill et al. (2008), 0806.0183.
 - [65] V. Acquaviva, A. Hajian, D. N. Spergel, and S. Das, *Phys. Rev. D* **78**, 043514 (2008), 0803.2236.
 - [66] L. Knox, *Phys. Rev. D* **52**, 4307 (1995).
 - [67] C. Carbone, L. Verde, and S. Matarrese, *Astrophys. J. Lett.* **684**, L1 (2008), 0806.1950.